Ultramafic-hosted Ni-Cu-Co-(As) mineralization from an ancient oceanic transform fault zone in the Troodos ophiolite, Cyprus: an analogue for ultramafic seafloor massive sulfide mineralization?

[1,2*]Andrew J. Martin, [3]Christopher J. MacLeod, [4]Katie A. McFall, [3]Iain McDonald, [1]John W. Jamieson and [3]Sophie Cox

[1] Department of Earth Sciences, Memorial University of Newfoundland, Canada

[2] Department of Geoscience, University of Nevada, Las Vegas, USA

[3] School of Earth and Environmental Sciences, Cardiff University, UK

[4] Earth Sciences, University College London, UK

[*]Corresponding author: Andrew J. Martin (Andrew.martin@unlv.edu)

Abstract

Accumulations of sulfide minerals that are enriched in Ni-Cu-Co-(As) occur as seafloor massive sulfide (SMS) deposits associated with ultramafic lithologies on the seafloor and in ophiolite terranes as Outokumpu-type mineralization. In this study we focus on similar mineralization at Lakxia tou Mavrou in the Limassol Forest Complex of Cyprus, which represents the on-land exposure of an oceanic transform fault zone preserved within the Troodos ophiolite. Mineralization here consists of massive lenses of pyrrhotite associated with veins of isocubanite, chalcopyrite, Co-pentlandite and chrome spinel hosted in serpentinized mantle peridotite. We re-examine the field context of mineral occurrences and use *in situ* mineral chemistry, element mapping and sulfur isotope ratios ($\delta^{34}S$) to constrain metal sources and provide an updated paragenetic model for Lakxia tou Mavrou. Highly variable S/Se ratios (304 to 108,571), a depletion in platinum group elements relative to mantle values and an average $\delta^{34}S$ value of -3.7±2.4‰ (1σ, *n=17*) in sulfide minerals support a hybrid hydrothermal and magmatic origin for the mineralization. Metals at Lakxia tou Mavrou were sourced from both the serpentinization of peridotites and from cross-cutting intrusions, with later intrusions into the already serpentinized mantle lithosphere host providing a heat

source to drive prolonged hydrothermal circulation. The re-examination of the field context of mineralization shows that the Ni-Cu-Co-(As) mineralization at Lakxia tou Mavrou originally formed as a consequence of the fault-guided intrusion of hot primitive magma bodies into serpentinized shallow mantle lithosphere in the active domain of an ocean-floor transform fault zone. The mineralization was subsequently partially disrupted by structures related to emplacement of the Troodos ophiolite. We show that the relationship between serpentinization, magmatism and hydrothermal circulation at Lakxia tou Mavrou can be used to understand the formation of ultramafic-hosted SMS deposits in transform fault and other ultramafic-dominated slow- and ultraslow-spreading mid-ocean ridge settings.

Introduction

Serpentinization of peridotites at and below the seafloor occurs during seawater circulation where primary igneous olivine and pyroxene are hydrated to form secondary minerals such as chrysotile, lizardite, antigorite and magnetite (Alt and Shanks, 2003; Mével, 2003). The destruction of olivine and pyroxene during serpentinization releases large quantities of Ni, Co and Fe that are hosted within these minerals. Simple cooling and serpentinization of peridotite is normally thought insufficient in itself to generate significant metal concentrations (Petersen et al. 2009; Allen and Seyfried, 2003). To form sulfide mineralization an additional heat source is required to drive high-temperature (~350°C) fluid circulation and to transport Ni, Co and Fe in hydrothermal fluids to the seafloor, potentially to form seafloor massive sulfide (SMS) deposits (Fouquet et al., 2010). Seafloor massive sulfide deposits from during the interaction of seawater with underlying magma chambers in oceanic crust where high-temperature (>350°C) seawater-derived hydrothermal fluid leaches metals from the underlying crust. The metals are then transported in the hydrothermal fluid and exhaled on the seafloor to form hydrothermal precipitates (e.g., Hannington et al. 2005). The study of SMS deposits is of particular interest as they represent actively-forming analogues to ancient volcanogenic massive sulfide (VMS) deposits that are preserved in ophiolite terranes (e.g., Peltonen

et al. 2008). However, the relationship between igneous intrusions, serpentinization and SMS deposit formation remains poorly characterized in both ancient and active deposits.

Environments in which areas of serpentinized mantle lithosphere are exposed at the Earth's surface are now known to be far more commonplace in the ocean basins than previously thought (Mével, 2003). Mantle-derived ultramafic lithologies, that are variably serpentinized, represent ~20-25% of the seafloor at slow- to ultra-slow spreading mid-ocean ridges (<40 mm a year), representing ~14,660 km of the present day ridge system (Cannat et al., 2010), principally along large-offset extensional detachment faults (e.g., Cannat, 1993; Cann et al., 1997). Ocean-floor serpentinization of the mantle appears also to be widespread at oceanic transform plate boundaries (e.g., Francis, 1981), where oceanic crust is thin, fractured and permeable. Increased permeability facilitates seawater circulation deep into the mantle lithosphere and promotes the serpentinization of lithospheric mantle peridotite (Francis, 1981; McCaig et al., 2007). Mafic igneous intrusions into mantle lithosphere have been documented in both detachment fault footwalls (e.g., 15°45'N on the Mid-Atlantic Ridge: MacLeod et al., 2002; Escartin et al., 2003, Atlantis Massif: Ildefonse et al., 2007) and in oceanic transform fault zones (e.g., Siqueiros transform zone: Fornari et al., 1989; Garrett transform zone: Hekinian et al., 1992). Spatially related SMS deposits occur both at or away from the spreading axis in ultramafic seafloor (e.g., Rona et al., 1987; Krasnov et al., 1995; Cherkashev et al., 2013; Petersen et al., 2009). For example, the Semenov-2 hydrothermal field at 13°30' N on the Mid-Atlantic Ridge forms ~5.5 km away from the spreading ridge axis (Escartin et al., 2017). However, no equivalent such deposits have been reported from oceanic transform faults, though there is potential for them to form in this tectonic environment, as the crust is highly permeable due to faulting and syn-tectonic magmatic intrusions can occur (Francis, 1981; Fornari et al., 1989; Hekinian et al., 1992).

Because of the technical and logistical challenges, little is known of the controls on sulfide mineralization in serpentinite-hosted seafloor environments. Potential insight may however be derived from the study of ophiolites. Numerous occurrences of Ni-Cu-Co-(As) mineralization are associated with ultramafic host rocks in ophiolite complexes. These are termed "Outokumpu-type" sulfide deposits (e.g., Bou Azzer,

Morocco), and could represent ancient analogues to ultramafic-hosted SMS deposits actively-forming along slow- and ultraslow-spreading mid-ocean ridges. However, linking the formation of Outokumpu-type deposits to seafloor processes remains speculative (e.g., Coltat et al., 2021). Examples of ultramafic-hosted occurrences on the modern seafloor include Ashadze, Logatchev, Semenov, Rainbow, Longqi-1, Kairei and Von Damm vent fields (Leblanc and Billaud, 1982; Fouquet et al., 1997; Peltonen et al., 2008; Petersen et al., 2009; Fouquet et al., 2010; Connelly et al., 2012; Melekestseva et al., 2014, 2020; Wang et al., 2018; Tao et al., 2020; Patten et al., 2022). These sulfide deposits are enriched in Ni and Co relative to deposits hosted in mafic environments (Hannington et al., 2005). By comparison, Outokumpu-type deposits contain higher contents of Ni, Cu and Co and have a higher tonnage relative to known ultramafic-hosted SMS deposits. For example, at Outokumpu, the ore reserve was 28.5 Mt at 3.8 wt.% Cu, 0.24 wt.% Co and 0.12% Ni (Parkkinen, 1997). With the exception of the Semenov hydrothermal field (13°30’ N, MAR) that has an estimated tonnage of 40 Mt, most other deposits are smaller, for example Ashadze at 5.2 Mt or Logachev at 1.9 Mt (Cherkashev et al., 2013). In ancient terranes, most Outokumpu-type deposits occur within highly metamorphosed regions (up to amphibole facies), in which primary mineral textures and geochemical signatures have been overprinted or modified during metamorphism (e.g., Bou Azzer, Morocco or Kylylahti, Finland; Leblanc and Billaud, 1982; Peltonen et al., 2008). Metamorphic upgrading of the deposits, where metals are remobilized and concentrated, is proposed to be an important process in achieving economic metal grades (Peltonen et al., 2008).

In this study we examine an occurrence of Ni-Cu-Co-(As) sulfide mineralization in serpentinized peridotite within a late Cretaceous oceanic transform fault preserved in the Troodos ophiolite of Cyprus. The mineralization, at the Lakxia tou Mavrou occurrence, may have partially formed by hydrothermal processes analogous to modern ultramafic-hosted SMS deposits. We investigate the geological setting of the mineralization and evaluate its comparability to similar hydrothermally active ultramafic settings on the modern ocean-floor and compare these to Outokumpu-type deposits. We find that sulfur isotope ratios, sample mineralogy, and elemental compositions are different between Lakxia tou Mavrou and a typical

Troodos mafic-hosted VMS deposit, and that these differences can be related to the specific tectonic setting of Lakxia tou Mavrou. Our findings confirm that Lakxia tou Mavrou did not form at the seafloor, but rather below the seafloor from hydrothermal processes generated by interactions of magma intrusions into already-serpentinized peridotite, forming a hybrid between SMS and Outokumpu-type deposits. We highlight the potential for replacement-type sulfide mineralization to form in ultramafic rocks deep below the seafloor and in associated ophiolite terranes.

Geological Background

The Troodos ophiolite

The Troodos ophiolite of Cyprus is a fragment of Cretaceous oceanic lithosphere (~92 Ma; Mukasa and Ludden, 1987) formed by seafloor spreading in a supra-subduction zone environment (Miyashiro, 1973; Pearce, 1975; Gass, 1980). The Troodos Massif preserves a complete Penrose stratigraphy: mantle peridotites are overlain by a continuous 4-5 km-thick oceanic crust comprising ultramafic and mafic plutonic rocks, a regionally extensive sheeted dyke complex and an extrusive lava sequence of arc tholeiite to boninite composition (e.g., Gass, 1968; Moores et al., 1971; Pearce and Robinson, 2010). Troodos was then later uplifted and exhumed in the Miocene (Robertson, 1977).

Arakapas Fault Belt and Limassol Forest Complex: the "Southern Troodos Transform Fault Zone"

The southern margin of the Troodos massif, the Arakapas Fault Belt and Limassol Forest Complex region, is characterized by more complex geological relationships than in the remainder of the ophiolite (Fig. 1A and B). The Arakapas Fault Belt and Limassol Forest Complex are generally accepted as forming part of a ≥5 km wide E-W trending syn-accretionary seafloor fault zone that represents an oceanic transform fault (Moores et al., 1971; Simonian and Gass, 1978) referred to as the Southern Troodos Transform Fault Zone (STTFZ). A small sliver of Anti-Troodos crust from the opposite plate is preserved in the southeastern

Limassol Forest Complex (MacLeod, 1990; Gass et al., 1994), and a fossil ridge-transform intersection lies to the present-day southwest of Mount Olympus (MacLeod et al., 1990).

The Arakapas Fault Belt forms the northern margin of the STTFZ (Fig. 1B), at paleo-seafloor level, prior to uplift and exhumation, and consists of an E-W trending zone of sheeted dykes and lavas cut by numerous braided fault strands of intense brittle strike-slip deformation, forming a laterally continuous zone of faulting extending for over 30 km E-W along strike (Simonian, 1975; Simonian and Gass, 1978; MacLeod and Murton, 1993; Fagereng and MacLeod, 2019).

The Limassol Forest Complex is characterized by deep erosional levels (~3-4 km; Murton et al., 1986a) geometrically complex dismembered, rotated and intercalated fault blocks from all stratigraphic levels, including extensive areas of serpentinized mantle peridotite (Fig. 1B). Across the western Limassol Forest Complex extensive deformation is manifested as high-strain, dextral strike-slip serpentinite shear zones up to hundreds of meters wide and traceable along strike for a few tens of km (Murton 1986a; MacLeod and Murton, 1993, 1995; Fagereng and MacLeod, 2019; Cox et al., 2021). These shear zones cut, but are themselves also cross-cut, by extensive syn-tectonic ultramafic and mafic magmatic intrusions of boninitic composition. These "Transform Sequence" intrusions take the form of plutons hundreds of meters to several km wide, accompanied by voluminous swarms of dykes (locally sheeted, and forming up to 22% of the local area: Murton, 1986a), that intrude already-serpentinized host mantle lithosphere, earlier "Axis Sequence" crustal blocks and shear zones (Murton 1986a, b; MacLeod and Murton, 1993, 1995; Gass et al., 1994). These relationships indicate transtension and magma focusing into a locally "leaky" active ocean-floor transform plate boundary (Murton 1986a; Gass et al., 1994). Significantly, the pervasive serpentinization of >3 km of the lithospheric mantle in the Limassol Forest Complex occurred prior to and during transform-related deformation and intra-transform magmatic intrusion and indicates deep, wholesale penetration of seawater into the active domain of the transform (Murton, 1986a, MacLeod and Murton, 1993, 1995; Cox et al., 2021).

Lakxia tou Mavrou

The Ni-Cu-Co-(As) mineralized zone at Lakxia tou Mavrou is located ~1.5 km south of the village of Dhierona (Fig. 1B). It lies within sheared, serpentinized mantle rocks of the western Limassol Forest Complex, near a faulted boundary with the sheeted dyke complex (Fig. 1B and C), and therefore within the original ocean-floor transform-tectonized domain and at relatively deep levels (~3-4 km) beneath the seafloor of the original transform fault valley. Its local geological setting is complex, due to multiple generations of seafloor and uplift related deformation but decipherable in the broader context of the tectonics of the Limassol Forest Complex (Gass et al., 1994).

On the 1:25,000 scale maps of Gass et al. (1994), Lakxia tou Mavrou is located within a ~300 m wide zone of E-W trending sheared serpentinite that, to the west, continues for several km (Fig. 1B and C). Serpentinized mantle peridotite forms the southern margin of this shear zone. To the north, sheeted dykes are indicated as forming the northern margin for the first kilometer west of Lakxia tou Mavrou and then serpentinized mantle peridotite farther to the west (Fig. 1C). To the east of Lakxia tou Mavrou, however, the serpentinite shear zone is marked as turning towards the ESE, and effectively merging with a broad, compound zone of WNW-ESE faulting termed the "Pevkos Fault" that can be traced ~11 km further to the ESE (Fig. 1C: MacLeod, 1990).

The Pevkos Fault has a protracted history, originally having a down-to-the-SSE sense of movement that cuts an earlier regionally extensive sub-horizontal detachment fault, the Akapnou Forest Décollement (AFD) that separates plutonic rocks and serpentinized peridotite (MacLeod, 1988, 1990; Gass et al., 1994; Fig. 1C). To the SE, the Pevkos Fault separates plutonic rocks from Anti-Troodos lavas, with ≥3 km total displacement (total crustal thickness of ~4km for Anti-Troodos: MacLeod, 1988). The Pevkos Fault is demonstrably younger than the transform-related E-W structures (Fig. 1C). From our own field investigations, we have ascertained that rather than merging in the vicinity of Lakxia tou Mavrou, WNW-trending faulting related to the Pevkos Fault zone instead cuts across the earlier E-W dextral strike-slip

shear zone. This is evident in local-scale geological maps of Lakxia tou Mavrou, in which broadly WNW to NW-striking fault or shear zones are shown to cut the area, including pre-existing sheared serpentinite (Fig. 1D: Panayiotou, 1980; BMG, 2013). Moreover, sheeted dykes do not form the northern margin to the transform-related E-W serpentinite shear zone to the east of Lakxia tou Mavrou (Fig. 1C). Instead, the contact between the dykes and serpentinite represents a westerly continuation of the same Akapnou Forest Décollement (Fig. 1C; MacLeod, 1990; Gass et al., 1994).

Mineralization at Lakxia tou Mavrou is preserved in the E-W serpentinite shear zone, where it is spatially associated with Transform Sequence intrusions. Greenschist facies, slightly rodingitized, hydrothermally altered boninitic dykes have been intruded into serpentinite, chilled and then sheared/boudinaged into cm to m-sized phacoidal blocks within the phyllonitic serpentinite shear zone (Fig. 2A). The dykes are also notable for containing 1-2% of 2-3 mm-diameter spherical sulfide blebs. The vertical E-W trending host serpentinite shear zone has dextral S-C shear sense indicators (Fig. 2B and C), with chrysotile forming the main serpentinite polymorph indicating that most deformation took place at temperatures in the range of 200-300°C (Cox et al., 2021). Textures in core samples of the sulfide mineralization itself indicate ductility (Fig. 2D, E and F), but pyrrhotite and chalcopyrite, which dominate here, have been shown to deform in this fashion at temperatures as low as ~100°C and ≤~200°C, respectively (Marshall and Gilligan, 1987 Cook et al., 1993; LaFrance et al., 2020).

The mineralized zone is characterized by massive, veined, and disseminated sulfide mineralization with trace amounts (<1 wt.%) of arsenide minerals (Foose et al., 1985; Thalhammer et al., 1986). Pyrrhotite, chalcopyrite, isocubanite, and pentlandite form the main sulfide minerals with trace amounts (<1 wt.%) of cobaltite (CoAsS), maucherite ($Ni_{11}As_8$), and löllingite ($FeAs_2$) (Panayiotou 1980). At the surface, a gossan of pyrrhotite and Fe-oxide outcrops and historic adits are accessible (Fig. 1D). Drilling of Lakxia tou Mavrou in 2013 by Brazilian Metals Group (BMG) produced intersections of 4.3 m at 2.5% Cu and 4.2 m at 1.7% Cu, 1.18 g/t Au and 0.15% Co (BMG, 2015). The mineralized package dips steeply (>60°) to the north and varies in thickness from 20-40 m wide with gossan exposures traceable for ~1.5 km along strike

(BMG, 2015). The morphology of sulfide mineralization varies along strike and spatially across the serpentinite shear zone, with massive lenticular sulfide bodies and veins more common to the north, and disseminated sulfide mineralization more common to the ESE at a smaller sulfide occurrence called Pevkos (~5km; Fig 1B; Panayiotou, 1980). The Pevkos deposit was, however, even more heavily disrupted and modified by the later tectonic events referred to in the preceding section and its original paragenetic relationships are less clear. In addition to a high-degree of deformation, mineralization at Pevkos was inaccessible at the time of study and hence is not considered further in this study.

Methods

Mineralogy

Reflected light microscopy was undertaken on representative polished mounts (*n=10*) prior to scanning electron microscope (SEM) analysis. Element mapping was performed on a Zeiss Sigma HD Automated Scanning Electron Microscope (ASEM) equipped with two Oxford Instruments X-Max^N 150 mm large area Silicon Drift Detectors at Cardiff University, UK. The SEM was operated using an accelerating voltage of 15 kV with a dwell time of 1500 ms at <200x magnification, yielding an average resolution of <3 µm. Data correction, deconvolution and element map construction was performed using Oxford Instruments Aztec software's TruMap function.

Mineral chemistry

Laser ablation inductively coupled plasma mass spectrometry (LA-ICP-MS) was carried out on representative polished mounts (*n=10*) to determine the *in situ* content of trace elements across different sulfide minerals. In total, 186 spot analyses were carried out across pyrrhotite (*n=69*), pentlandite (*n=34*), chalcopyrite (*n=38*), and isocubanite (*n=45;* App. Table A1). LA-ICP-MS analysis was performed at Cardiff University (UK) using a New Wave Research UP213 UV laser coupled to a Thermo iCAP RQ-ICP-MS. Analysis employed a spot diameter of 55 µm at a frequency of 10 Hz and a gas blank was measured for 20 s prior to each analysis. Sulfur-33 was used as an internal standard for all analyses and instrument

calibration was performed on a series of synthetic Ni-Fe-S standards (see Prichard et al., 2013; Smith et al., 2016). Data quality was monitored through the repeat analysis of UQAC FeS-1 with calculated relative standard deviation (RSD) values of <6% for Fe, Ni, Cu, As, Ru, Ag, Te, Re Ir, <10% for Co, Se, Rh, Pt, Pd, Os, Au and Bi and an RSD of <16% for Zn, Pd, Cd, Sb and Pb (see App. Table A1). Data correction and the subtraction of gas blanks was performed using Thermo Qtegra software.

Sulfur isotope analysis

The sulfur isotope composition of pyrrhotite and chalcopyrite was determined using secondary ion mass spectrometry (SIMS) microanalysis. Twenty-three analyses were performed across three representative polished mounts. Epoxy-mounted blocks with aluminum retaining rings were first coated with 300Å of Au prior to analysis to mitigate charging of the sample during ion bombardment. Samples were analyzed using a Cameca IMS 4f SIMS instrument at the Microanalysis Facility at Memorial University of Newfoundland (Canada) following the analytical procedure detailed in Brueckner et al. (2015) and Lode et al. (2017). The sample was bombarded with a primary ion beam of 350-750 pA of Cs^+, accelerated through a potential of 10 KeV and focused into a 5-15 μm diameter rastered spot. Negatively charged secondary ions were accelerated into the mass spectrometer using a potential of +4.5 KeV. To exclude sulfur contamination from the sample surface, the analytical spot was sputtered for 120 s with a 5-15 μm diameter rastered beam prior to analysis. All analyses are reported in standard delta notation ($\delta^{34}S$, ‰) relative to Vienna-Canyon Diablo Troilite (V-CDT). Reproducibility based on the repeat analysis of standard reference material UL9 ($\delta^{34}S$= 16.3‰), KH87 ($\delta^{34}S$= 0.4‰) and PoW1 ($\delta^{34}S$= 3.0‰) is better than 0.4‰ (1σ, see App. Table A2).

Sample preparation and analysis of Platinum Group Elements

Samples were prepared for PGE analysis by nickel sulfide fire assay pre-concentration and tellurium co-precipitation at Cardiff University, as described in Huber et al. (2001), but incorporating the modifications outlined in McDonald and Viljoen (2006). Solutions were then analyzed for PGE and Au on a Thermo iCAP RQ-ICP-MS at Cardiff University (UK). Accuracy and precision was assessed by the repeat analysis of PGE reference material WPR-1 (altered peridotite) (App. Table A3).

Results

Mineralogy

Samples from Lakxia tou Mavrou are sub-divided based on texture into veined (Fig. 2 E and F) and massive samples (Fig. 2G). Veined samples occur surrounding massive sulfide lenses and contain a mesh of sulfide-rich veins in a serpentinite matrix (Fig. 2E and F). Massive samples contain >95% sulfide minerals, with minor magnetite, chromite, arsenide minerals and serpentinite (Fig. 2G).

Massive samples. Massive samples contain pyrrhotite (>95%) with disseminated pentlandite (<5%), chalcopyrite (<3%) and accessory amounts of chrome spinel, isocubanite, magnetite, and arsenide minerals (<<1%; see As map in App. 4) (Fig. 3). Pyrrhotite is cross-cut by magnetite-bearing breccia zones (Fig. 3A and 4) forming along 1-2 mm wide bands of brittle deformation that are surrounded by halos of fingerprint textured ductilely deformed pyrrhotite (Fig. 3B). Isocubanite occurs as exsolution lamella in chalcopyrite (Fig. 3C). Chrome spinel occurs as coarse (<0.5 mm) euhedral grains that are disseminated in pyrrhotite with some grains exhibiting alteration to ferri-chromite at their margins (Fig. 3D). Pentlandite is finely disseminated throughout the sample and occurs spatially associated with pyrrhotite (Fig. 3E).

Veined samples. Samples contain isocubanite, chalcopyrite, pentlandite, and pyrrhotite in a matrix of sheared serpentinite (Fig. 4A and B). Chrome spinel occurs as euhedral grains both surrounded by sulfide minerals (Fig. 4C) and associated with serpentinite (Fig. 4D). Some chrome spinels are anhedral with a pitted appearance and have a rim of ferri-chromite alteration (Fig. 4D). Isocubanite is often overgrown by chalcopyrite at its contact with surrounding serpentinite (Fig. 4E). Chalcopyrite also occurs within massive isocubanite as orientated exsolution lamella and as later overgrowths forming euhedral grains (Fig. 4F). Pentlandite occurs in pyrrhotite as discrete micron-scale subhedral grains with a feathery appearance (Fig. 4G and H). Mesh textures of pyrrhotite and chalcopyrite are common (Fig. 4 I, J and K). Some sulfide grains are fragmented and cross-cut by serpentinite veins. This indicates that brittle deformation of sulfide minerals took place late in the deposit paragenesis (Fig. 4L).

The relationship between sulfide minerals and serpentinite is variable within and between individual samples (Fig. 5). Clear mineralogical relationships exist between the different minerals in veined samples. Pentlandite is spatially associated with pyrrhotite, occurring as euhedral grains (Fig. 5A). Isocubanite occurs in massive zones (Fig. 5A and B) with patchy overgrowths of chalcopyrite (Fig. 5B). The majority of chalcopyrite occurs localized along shear bands (Fig. 5C). Chrome spinel occurs in all samples as discrete aggregates associated with serpentinite (Fig. 5). For individual maps of each analyzed element, refer to Appendix 4.

In veined samples, mesh textures are common, and consist of anastomosing networks of mm-scale veins containing pyrrhotite and chalcopyrite cross-cutting the serpentinite matrix that grade into coherent massive pyrrhotite and isocubanite (Fig. 5A and B). Evidence of deformation is visible where serpentinite cross-cuts and offsets pyrrhotite, indicating that displacement has occurred along a shear surface (Fig. 5A). In other samples, discrete bands of chalcopyrite within serpentinite (+/- chrome spinel) cross-cut isocubanite and pyrrhotite (Fig. 5C). Clasts of serpentinite within these zones appear to have a crude sigmoidal shape indicating that localized ductile deformation has occurred post sulfide formation (Fig. 5C), likely during later NNW-ESE faulting associated with the Pevkos fault.

Dyke-hosted sulfide globules. Dykes that intrude serpentinite in the vicinity of Lakxia tou Mavrou (Fig. 2A) contain disseminated poly-sulfide globules. Pyrrhotite, chalcopyrite and pentlandite occur in sub-rounded globules 2-3 mm in diameter (Fig. 6). One sulfide globule contained predominantly chalcopyrite (Fig. 6A) whilst all others contain only pyrrhotite with chrome spinel (Fig. 6B). Pentlandite was not visible in any sample but sub-micron-scale Ni-rich inclusions that are probably pentlandite were visible in some element maps (Fig. 6C). Euhedral chrome spinel grains occur disseminated within the sulfide globules and in the zone surrounding the globule (Fig. 6). A halo of Mg-rich alteration of approximately 0.5 to 1 mm wide mantles all poly-sulfide globules (Fig. 6).

Mineral chemistry

Variations in trace element concentrations are observed between pyrrhotite (*n=62;* spot analyses), pentlandite (*n=34*), chalcopyrite (*n=38*), isocubanite (*n=45*) and dyke-hosted pyrrhotite (*n=6*). All analyses returned Ru, Rh, Pd, Os, Ir and Pt concentrations below the detection limit (0.05 to 0.08 ppm). Metal contents below the detection limit are taken as half the detection limit (see App. Table A1).

Pyrrhotite. Median contents of Ag, Cd, Sb, As, Pb and Au are below the detection limit in pyrrhotite. Pyrrhotite contains the lowest median Se and Te content at 111 ppm and 0.41 ppm (*n=62*), respectively (Fig.7 A and B) and the second highest median Co content and Ni at 349 ppm and 0.17 wt.% (*n=62*; Fig. 7D and F), respectively. A strong positive correlation exists between Co and Ni (R^2=0.91; Fig. 7G).

Chalcopyrite. Chalcopyrite contains the highest median Te, Se, Cd, Sb and Zn contents (Fig. 7). Selenium is notably enriched with a median content of 213 ppm (*n=38*) and a maximum of 934 ppm (Fig. 7A). Chalcopyrite has the highest median Te content at 23 ppm (*n=38*; Fig. 7B). A strong positive correlation exists between Co and Ni (R^2 = 0.94; Fig 7G), Zn and Cd (R^2=0.95; Fig. 7H) and a weak correlation between Te and Se (R^2=0.58).

Isocubanite. Isocubanite contains a median Cu content of 25 wt.% (*n=45*; Fig 7E). Isocubanite, with a median content of 1.3 ppm (*n=45*) is enriched in Ag relative to all other sulfide minerals analyzed. Isocubanite is depleted in Se relative to chalcopyrite, with a median of 165 ppm (*n=45*; Fig. 7A). A strong positive correlation exists between Co and Ni (R^2=0.85; Fig. 7G) and Cd and Zn (R^2=0.84; Fig. 7H).

Pentlandite. Pentlandite contains the highest median Bi, Sb and As content at 1.0 ppm (Fig. 7C), 0.23 ppm, and 22 ppm (*n=34*), respectively. The Ni content of pentlandite ranges from 12.7 to 20.7 wt% with a median of 14.6 wt.% (*n=34*; Fig. 7D). Pentlandite contains an average Co concentration of 33.0 ± 5.9 wt.% (1σ, *n=34;* 10F). Based on a Co content >20 wt.%, we classify pentlandite as Co-pentlandite (Harris and Nickel, 1972). A strong positive correlation occurs between Ni and Fe (R^2 = 0.89) and a moderate negative correlation between Fe and As (R^2=-0.69).

Dyke Pyrrhotite. Dyke-hosted pyrrhotite has a different trace element signature compared to Lakxia tou Mavrou pyrrhotite, having a higher Ni, Co, Se, Te and Pb content. Arsenic is enriched in dyke-hosted pyrrhotite, with a median content of 66 ppm (*n=6*), compared to Lakxia tou Mavrou pyrrhotite, where all analyses were below the detection limit (<1.1 ppm). Nickel, with a median content of 5641 ppm (*n=6*), is also enriched relative to Lakxia tou Mavrou pyrrhotite. Concentrations of Cd, Zn, Cu, Ag and Au are below the detection limit for all analyses. Arsenic exhibits a strong positive correlation with Ni (R^2=0.94) and a moderate positive correlation with Co (R^2=0.60).

Sulfur isotopes

Sulfur isotope ratios ($\delta^{34}S$) were measured on pyrrhotite from veined and massive samples (*n=9*) and the sulfide blebs in the boninite dykes from the serpentinite shear zones (*n=6*) (Fig. 8). Pyrrhotite in massive samples has an average $\delta^{34}S$ value of -1.8±1.4‰ (1σ, *n=4*; Fig. 8) and pyrrhotite from veined samples -2.5±1.5‰ (1σ, *n=5*). In contrast, the dyke-hosted pyrrhotite is relatively enriched in ^{34}S, having an average $\delta^{34}S$ value of 14.7±4.3‰ (1σ, *n=6*) and a maximum value of 20.9‰ (Fig. 8). Chalcopyrite in massive samples is depleted in ^{34}S with an average $\delta^{34}S$ value of -6.1±2.0‰ (1σ, *n=5*) relative to veined samples at -4.4±2.3‰ (1σ, *n=3*) (Fig. 8).

Whole rock PGE analysis

Whole rock samples from massive sulfide, veined samples, and from the boninite dykes were analyzed (*n=6*). All samples have PGE concentrations that are lower than mantle values (mantle values from Palme and O'Neill, 2003) and only the massive sulfide samples contain Au above mantle values. Massive and veined samples have similar PGE patterns: flat with a slight positive inflection at Ru, and a strong Au enrichment. However, the massive samples contain higher concentrations of Ir, Os, Rh, Pt and significantly higher concentrations of Au than the veined samples (Fig. 9). Massive samples have an average Pt/Pd ratio of 1.2, Au/Pd ratio of 190.2 and Pd/Ir ratio of 1.7, while veined samples have an average Pt/Pd ratio of 0.8, Au/Pd ratio of 13.6 and Pd/Ir ratio of 5.5. Boninite dyke samples contain notably less PGE than the mineralized samples and have a different pattern, with a positive Pt inflection and then a depletion in Au

and Pd. Samples from the dykes have an average Pt/Pd ratio of 4.0, Au/Pd ratio of 0.1 and Pd/Ir ratio of 22.1 (Fig. 9; App. Table A3).

Discussion

Magmatic versus hydrothermal origins

Previous studies have suggested either a magmatic (Panayiotou, 1980) or hydrothermal (Foose et al., 1985; Thalhammer et al., 1986) origin for mineralization at Lakxia tou Mavrou. Mineralization was considered to have formed through magmatic processes via the segregation of an immiscible sulfide liquid during the ascent of basaltic melts through the lower crust (Panayiotou, 1980). This genetic model was based primarily on the absence of a hydrothermal alteration halo surrounding the sulfide mineralization and the enrichment of Cu with Cu/Cu+Ni of between 0.16 and 0.47 (Panayiotou, 1980).

Later studies have suggested a hydrothermal origin for the mineralization, where metals are sourced from the serpentinization of mantle peridotites (Foose et al., 1985; Thalhammer et al., 1986). If mineralization were formed via purely magmatic processes, as suggested by Panayiotou (1980), it would be expected to have a Pt/(Pt+Pd) ratio of between 0.2 and 0.4; however Pt/(Pt+Pd) ratios are elevated at Lakxia tou Mavrou, ranging between 0.51-0.66 (Foose et al., 1985). Sulfide mineralization is also depleted in PGEs relative to Troodos gabbros and peridotites, with a flat PGE profile and a sharp increase in Au, again suggesting a hydrothermal origin (Foose et al., 1985). Thus, a two-step hydrothermal model explaining the formation of Lakxia tou Mavrou sulfide mineralization was instead proposed: (i) high-temperature fluids (400-500°C) formed pyrrhotite-rich mineralization with co-precipitated arsenide minerals followed by, (ii) a lower temperature (200-300°C) fluid that precipitated Cu-rich sulfide minerals (Thalhammer et al., 1986).

All of these models were proposed before detailed mapping and geological investigation of the Limassol Forest Complex (Murton, 1986a, b; MacLeod, 1988, 1990; MacLeod and Murton 1993, 1995; Gass et al., 1994), and without the benefits these studies brought in deciphering the detailed geological context of the

Lakxia tou Mavrou area. The origin and paragenesis of the mineralization is re-evaluated in this study by applying a combined mineralogical, geochemical and isotopic approach.

Evidence of a hydrothermal origin for Lakxia tou Mavrou

Firstly, S/Se ratios are commonly used to constrain the source of sulfur in magmatic and hydrothermal ore deposits (Yamamoto, 1976; Queffurus and Barnes, 2015; Smith et al., 2016). The S/Se ratio of the mantle is between 2850 to 4350 (Eckstrand and Hulbert, 1987). At Lakxia tou Mavrou the median S/Se for all sulfide minerals are 2293 (*n=180*) with a range of 304 to 108,571, which is comparable to hydrothermal mineral deposits where the S/Se ratios range from 3500 to 100,000 (Yamamoto, 1976; Huston et al., 1995; Hannington et al., 1999; Layton-Matthews et al., 2013). Therefore, S/Se ratios that are highly variable and plot both above and below mantle values support a hydrothermal origin for mineralization at Lakxia tou Mavrou.

The sulfur isotope composition of Troodos mantle rocks is between 0-1‰ (Alt 1994). Therefore, if mineralization at Lakxia tou Mavrou did form through magmatic processes, then the sulfur isotope composition of sulfide minerals should also be similar (e.g., Smith et al., 2016). Instead, the average $\delta^{34}S$ values for all sulfide minerals analyzed in this study is -3.7±2.4‰ (1σ, *n=17*) ranging from -7.9‰ to -0.1‰, values that are largely not compatible with a magmatic origin (Smith et al., 2016).

Additional whole-rock PGE concentration data for veined, massive, and dyke-hosted sulfide globules also support a hydrothermal origin for Lakxia tou Mavrou (Fig. 9). Massive and veined samples have a similar chondrite-normalized PGE profile with a positive Ru inflection and slight negative inflection at Pt and both massive and veined samples are enriched in Au relative to primary Troodos host rocks. Platinum/(Pt+Pd) values for Lakxia tou Mavrou sulfides from this study range from 0.39 to 0.55 (average = 0.50, *n=4*) and are in good agreement with two previously published values of 0.51 and 0.66 (Naldrett et al., 1979; Foose et al., 1985). Platinum group element data (Table 2) indicate that the sulfide minerals are depleted in PGE

when compared to mantle concentrations, further supporting the premise that the sulfide minerals are either of hydrothermal origin or have been leached during later hydrothermal processes (Naldrett et al., 1979).

These data indicate that mineralization at Lakxia tou Mavrou does not have a simple magmatic origin through the segregation of an immiscible sulfide liquid. However, the relationship between serpentinization, faulting, fluid flow, the formation of sulfide mineralization and source of metals remain poorly constrained. To investigate this further we conducted *in situ* geochemical and sulfur isotope analysis, and draw comparisons between SMS deposits hosted in ultramafic rocks, Outokumpu-type VMS deposits and Lakxia tou Mavrou to examine if mineralizing processes are comparable.

Metal and sulfur sources at Lakxia tou Mavrou

Serpentinization. Serpentinization, which occurs when primary olivine and pyroxene are hydrated to from secondary minerals such as lizardite, chrysotile and magnetite, produces geochemically distinct fluids (Klein and Bach, 2009). Fluids produced during serpentinization are highly reduced, alkaline and have a low fS_2 (e.g., Allen and Seyfried, 2003). Serpentinization reactions are exothermic (MacDonald and Fyfe, 1985) and may drive hydrothermal fluid circulation (Rona et al., 1987). Modeling indicates that serpentinization can produce temperatures of up to ~260 °C, however, low fluid flow rates ($\leq$10 kg/s) or high rates of serpentinization ($\geq$ 100 kg/s) are required to reach these temperatures (Lowell and Rona, 2002). To achieve temperatures of >300°C, similar to temperatures recorded in basalt-hosted SMS systems (Hannington et al., 2005) an additional heat source (i.e., magmatic intrusions) is needed (Lowell and Rona, 2002). For example, even at the Lost City hydrothermal field (MAR: Denny et al., 2016; Kelley et al., 2001; Früh-Green et al., 2003) low-temperature (~40-91°C), high-pH (9-9.8) and metal-poor fluids are thought to be influenced by the presence of mafic intrusions (Allen and Seyfried, 2004). In ultramafic-hosted vent sites where fluid temperatures are higher due to the presence of mafic intrusions below the seafloor (e.g., Rainbow; 364°C), high H_2 contents (16 mmol/kg) have been measured in vent fluid, that are produced during serpentinization (Charlou et al., 2002). In these higher temperature systems, accumulations of sulfide minerals occur at the seafloor (e.g., Rainbow, Logatchev, Semenov). Sulfide accumulation reflects the

409 increased solubility of many metals (e.g., Cu) in high-temperature and low-pH hydrothermal fluid
410 (Rainbow; 365°C, pH 2.8; Charlou et al., 2002) (Palandri and Reed, 2004). Consequently, low-S, high-Fe
411 mineral assemblages containing isocubanite and pyrrhotite form due to the occurrence of reduced, sulfur
412 poor fluids, and have been reported in some ultramafic-hosted SMS deposits (Firstova et al., 2016).
413 Serpentinization in the STTFZ occurred on/below the ocean-floor and has been discussed in detail by
414 Murton (1986a,b), MacLeod & Murton, (1993, 1995) and Gass et al. (1994). Hence, in the context of
415 mineralization at Lakxia tou Mavrou, serpentinization could provide a source of metals.

416 The mineral assemblage, consisting of pyrrhotite and isocubanite (+/- chalcopyrite) at Lakxia tou Mavrou
417 indicates that fluids had a low fS_2 and were highly-reduced, favoring the formation of pyrrhotite over pyrite,
418 and isocubanote over chalcopyrite (Klein and Bach, 2009; Firstova et al., 2016). The highly reducing fluid
419 conditions are a consequence of serpentinization and redox reactions related to olivine and orthopyroxene
420 dissolution (Moody, 1976). At Lakxia tou Mavrou the pyrrhotite-rich sulfide mineral assemblage indicates
421 the involvement of high-temperature (200-500°C) highly-reduced fluids (Thalhammer et al., 1986), and
422 consequently, an additional source of heat at Lakxia tou Mavrou, in the form of gabbroic intrusions and
423 cross-cutting dykes is needed to produce sufficient amounts of heat to form sulfide mineralization.

424 Geochemical proxies such as the ratio of Co/Ni in Lakxia tou Mavrou sulfide minerals support the
425 contribution of metals from an ultramafic source (e.g., Marques et al., 2006). The median Ni and Co content
426 of pyrrhotite at Lakxia tou Mavrou is 68 and 178 times higher (Table 1), respectively for Ni and Co
427 compared to the median content in pyrite from all Troodos VMS deposits (*n=1376*; Keith et al., 2016;
428 Martin et al., 2019, 2020). This reflects the higher primary content of Ni and Co in peridotites, globally,
429 with mean concentrations of 2,344 ppm and 109 ppm, respectively (Gülaçar and Delaloye, 1976) compared
430 to mid-ocean ridge basalts that contain 92 ppm and 43 ppm Ni and Co, respectively (Gale et al., 2013). The
431 enrichment of Ni and Co at Lakxia tou Mavrou relative to basaltic-hosted VMS deposits provides evidence
432 for hydrothermal fluids at high-temperatures (>300°C) interacting with ultramafic lithologies.

At Lakxia tou Mavrou the average Co/Ni ratio for pyrrhotite is 3.4 (*n=62*), whilst the Co/Ni ratio from pyrite at Skouriotissa, a basalt-hosted VMS deposit in Troodos is 6.9 (*n=43*; Martin et al., 2019) (Fig. 10). Thus, the low Co/Ni ratio of pyrrhotite at Lakxia tou Mavrou combined with their elevated concentration, relative to the Skouriotissa VMS deposit, supports the contribution of metals from an ultramafic source rock. The average Co/Ni ratio of 3.4 (*n=62*) that lies between peridotite and mafic lithologies indicates a mixed mafic and ultramafic source of metals at Lakxia tou Mavrou (Fig. 10).

The role of mafic intrusions. In the western Limassol Forest, in the broader vicinity of Lakxia tou Mavrou, Transform Sequence wehrlite and gabbro plutons, plus associated (locally sheeted) swarms of boninitic dykes intrude into the serpentinized mantle, in places accommodating up to 22% of extension (Fig. 1B; Murton, 1986a; Gass et al., 1994). Transform Sequence dykes and gabbroic intrusions are clearly significant locally as a source of heat and metals (Murton 1986a, b; MacLeod and Murton, 1993, 1995; Gass et al., 1994). Early Transform Sequence dyke generations provide evidence of interaction with high-temperature (~350°C) hydrothermal fluids and are altered to greenschist to lower amphibolite facies (Murton et al., 1986a). Mass balance calculations in the main Troodos Massif show that at greenschist temperatures, metals are effectively leached from dyke material (Jowitt et al., 2012), hence, we suggest similar such processes occurred in the vicinity of Lakxia tou Mavrou with mafic intrusions providing an additional source of some metals.

Mafic lithologies may have also played an important role in lowering fluid pH and thus enhancing metal solubility (Palandri and Reed, 2004). This relates to the formation of chlorite, drawing Al from mafic lithologies and Mg^{2+} from seawater, producing H^{+} ions, lowering the pH of the hydrothermal fluid (Seyfried and Mottl, 1982). This reaction can overwhelm the brucite buffer that occurs during serpentinzation, and in addition to heat generated from the intrusion itself, will enhance the solubility of metals in the hydrothermal fluid (Palandri and Reed, 2004). Chloritization is prominent in gabbro intrusions, wehlrlite bodies and cross-cutting Transform Sequence dykes in the Limassol Forest Complex indicating that the formation of chlorite was an important mechanism in producing low-pH hydrothermal fluids.

458 Data from this study provides further evidence of hydrothermal alteration in the syn-tectonic boninitic
459 Transform Sequence dykes. The sulfur isotopic signature of disseminated pyrrhotite hosted within
460 Transform Sequence dykes (14.7±4.3‰ 1σ, max = 20.9‰; *n=6*) are distinctly different from both Troodos
461 VMS deposits, sulfide minerals at Lakxia tou Mavrou and the magmatic mean for Troodos igneous rocks
462 (0-1‰; Alt 1994) (Fig. 8). If these sulfide globules formed through primary magmatic processes then the
463 $\delta^{34}S$ values should plot around the Troodos magmatic mean of 0-1‰ (Alt 1994). Instead the average $\delta^{34}S$
464 value in pyrrhotite is significantly higher, indicating that the sulfide globules cannot be of a simple
465 magmatic origin. Furthermore, the dykes have a positive chondrite normalized PGE slope but are depleted
466 in Pd and Au relative to Lakxia tou Mavrou bulk-rock massive and veined samples (Fig. 9). These PGE +
467 Au signatures are different to those analyzed in sulfide-bearing gabbros from the main Troodos Massif,
468 which exhibit a positive slope with a trough in Ru and a peak in Pd relative to the dykes in this study
469 (Prichard and Lord, 1990; Fig. 9). Therefore we deduce that the geochemical signature of the sulfide
470 globules in the dykes must have been modified during the leaching of metals during hydrothermal alteration
471 and rodingitization, leaving globules depleted in PGE relative to primary magmatic sulfide minerals.
472 Alteration halos surrounding the sulfide globules (Fig. 6) further support that leaching and replacement has
473 occurred. Thus, we suggest that hydrothermal alteration of mafic intrusions provided an additional source
474 of metals, heat and probably played an important role in lowering fluid pH during the formation of sulfide
475 mineralization at Lakxia tou Mavrou.

476 *Sulfur sources*. The sulfur isotopic composition of sulfide minerals at Lakxia tou Mavrou is below the
477 Troodos magmatic mean of 0-1‰ (Alt 1994). An average $\delta^{34}S$ value of -3.7±2.4‰ (1σ, *n=17*) is not
478 compatible with sulfur sourced from a mixture of thermochemical sulfate reduction (TSR) of seawater and
479 the leaching of sulfur from igneous lithologies without any additional fractionation processes, as this would
480 produce sulfide minerals with $\delta^{34}S$ values >0‰, such as those measured in ultramafic-hosted SMS deposits
481 (Fig. 11).

Measured $\delta^{34}S$ values in pyrite that are lower than the Troodos magmatic mean have previously been documented at the basalt-hosted Mala VMS deposit (Troodos), where the median $\delta^{34}S$ value of pyrite is -4.6‰ (*n=28,* Martin et al., 2021) (Fig. 11). At Mala, that is interpreted to represent an immature VMS deposit, SO_2 from degassing shallow magma chambers undergoes disproportionation, producing low $\delta^{34}S$ values in pyrite that are <0‰ (Martin et al., 2021). The addition of a magmatic volatile phase to the hydrothermal system at Lakxia tou Mavrou is unlikely as mineralization is associated with ultramafic lithologies that are volatile poor (especially with respect to SO_2) relative to felsic lithologies. However, the addition of magmatic volatiles cannot be excluded as boninitic dykes that occur surrounding Lakxia tou Mavrou could potentially contribute magmatic volatiles. We do not consider microbial sulfate reduction (MSR) of seawater or sulfur leached from igneous host rocks at Lakxia tou Mavrou as a plausible source of isotopically light sulfur, as MSR occurs at low-temperatures (<<~122°C; Takai et al., 2008) that are not consistent with the high-temperature (>200°C) sulfide mineral assemblage at Lakxia tou Mavrou.

At Lakxia tou Mavrou sulfur isotope ratios of sulfide minerals increase from -7.9‰ in massive sulfide mineralization to 20.9‰ in dyke-hosted sulfide globules and are evidence of increasing amounts of TSR at different stages along a fluid pathway through the crust. As seawater penetrates down the shear zone it becomes heated by underlying magmatic intrusions and, at temperatures >150°C, anhydrite precipitation occurs (Fig. 12; Blounot and Dickson, 1969). Any remaining sulfate in the hydrothermal fluid is transported to deeper crust levels and, at temperatures >250°C and in the presence of iron-bearing minerals, is thermochemically reduced to H_2S (Machel et al., 1995). The equilibrium isotopic fractionation between SO_4^{2-} and H_2S is temperature dependent, with a greater degree of fractionation occurring at lower temperatures (Ohmoto and Rye, 1979). The amount of fractionation between H_2S, pyrrhotite and chalcopyrite is typically <0.8‰ at temperatures >300°C and is therefore minor (Li and Liu, 2006). During the TSR process, degree of progress of the sulfate reduction can be expressed in terms of *f* values, where $f = [H_2S]_{SR}/[SO_4]^0$, and $[H_2S]_{SR}$ denotes H_2S generated during TSR and $[SO_4]^0$ is the initial sulfate concentration of the fluid (Dubinina et al., 2020; Ono et al., 2012).

Low sulfur isotope values (<0‰) at Lakxia tou Mavrou are produced during the initial stage of TSR at low *f* values (~0.1) where only a small proportion of the sulfate entering the hydrothermal system undergoes TSR (Fig. 12). Equilibrium fractionation factors between SO_4^{2-} and H_2S are 22.2‰ at a temperature of 300°C (Sakai, 1968), forming sulfide minerals with negative $\delta^{34}S$ values down to -7.9‰ at Lakxia tou Mavrou (Fig. 12). Continued TSR (i.e., increasing *f* values) of the same fluid enrich the remaining sulfate in ^{34}S relative to the initial composition of seawater sulfate (~18-19‰; Kampschulte and Strauss, 2004). Continued TSR in a semi-closed system (with respect to seawater recharge) forms sulfide minerals with increasingly higher $\delta^{34}S$ values as sulfate that undergoes TSR is progressively enriched in ^{34}S but the equilibrium fraction factor remains constant at a given temperature (i.e., ~22.2‰ at 300°C). High $\delta^{34}S$ values such as those reported in dyke-hosted pyrrhotite globules that average 14.7±4.3‰ (1σ, *n=6*) are produced by near complete TSR at high *f* values (*f*= ~0.9). Therefore, variation in $\delta^{34}S$ values between sulfide minerals at Lakxia tou Mavrou and dyke-hosted pyrrhotite indicate progressively greater degrees of TSR in a semi-closed system that occurred along a fluid flow pathway (Fig. 12). At Lakxia tou Mavrou only the initial and end stage of TSR, representing low (~0.1) and high (~0.9) *f* values, respectively are preserved. Intermediate *f* values that will form sulfide minerals with $\delta^{34}S$ values of between ~0-10‰ are absent in the samples analyzed. We propose that the absence of these values is due to a sampling bias and suggest that values between 0-10‰ would be preserved in more distal parts of the mineralization, possibly toward Pevkos. Thus, the sulfur isotope composition of sulfide minerals at Lakxia tou Mavrou remains somewhat enigmatic, nevertheless we show that sulfur isotope systematics are distinctly different to those typical of actively-forming ultramafic SMS deposits and other basalt-hosted Troodos VMS deposits.

Sulfide mineralization in an ancient transform fault zone

Initially metals at Lakxia tou Mavrou were sourced from the serpentinization of peridotites in the vicinity of E-W trending vertical strike-slip shear zones, where seawater preferentially exploited the increased permeability related with deep-seated fault structures during fault movement from a very early stage (Fig. 13 - T1; MacLeod and Murton, 1993; Fagereng and MacLeod, 2019; Cox et al., 2021). The heat generated

during exothermic serpentinization reactions was insufficient to form significant accumulations of massive sulfide mineralization. Despite the relatively low-temperatures (<100°C), Ni and Co would have been leached during serpentinization (Fig. 13; T1).

Transform Sequence wehrlitic and gabbroic plutons and associated dyke swarms were intruded into already pervasively serpentinized peridotites in the vicinity of E-W trending transform shear zones in the lithospheric mantle. Decompressive partial melting was generated during trans-tension within/across the active transform portion of the STTFZ and intrusions provided an additional source of heat that drove convection of seawater-derived hydrothermal fluids. This produced an initial high-temperature (400-500°C; Thalhammer et al., 1986) stage of pyrrhotite-rich mineralization at Lakxia tou Mavrou (Fig. 13; T2). The solubility of Ni and Co, which had been liberated to form sulfide mineralization as a result of earlier and ongoing serpentinization increases at high-temperatures and low fluid pH as both Ni and Co possess an increased affinity for fluids >350°C (Liu et al., 2011, 2012). In addition to the mobilization of metals released during serpentinization, the addition of some metals from Transform Sequence intrusions (gabbros, wehrlites and dykes) also occurred (Fig. 13; T2). Within the roof zone of gabbroic stocks, aplite apophyses exhibit evidence of pervasive hydrothermal alteration with primary minerals being replaced by epidote, chlorite and actinolite (Murton 1986b), thus providing evidence that gabbroic plutons in the vicinity of Lakxia tou Mavrou (Fig. 1B and C) could have provided a source of metals.

Precipitation of sulfide minerals occurred in areas of increased permeability where seawater-derived hydrothermal fluids mixed with a down welling lower temperature seawater-derived fluid in the vicinity of E-W trending shear zones (Fig. 13; T2 inset image). This led to a decrease in fluid temperature and an increase in pH and fO_2 precipitating sulfide minerals. The continued intrusion of Transform Sequence dykes, that are variably altered from early amphibolite-greenschist dykes to brownstone facies dykes (Murton et al., 1986a) indicate prolonged hydrothermal and magmatic activity (Fig. 13; T3). As the initial gabrro and wehrlite intrusions cooled, ongoing dyke intrusions provided both a source of heat that drove prolonged high-temperature (>250°C) fluid circulation as well as providing an additional source of metals

(e.g., Cu) and buffering fluid pH to low values (~2) due to Mg sequestration from seawater derived hydrothermal fluids . Early Ni and Co-rich mineral assemblages are overprinted by isocubanite and later by chalcopyrite (Fig. 13; T3). The transition towards more Cu-rich mineral assemblages indicates a decrease in the temperature of hydrothermal circulation from ~400°C to ~250°C and the introduction of a higher proportion of metals sourced from Transform Sequence dykes that were intruded contemporaneously with the formation of Cu-rich sulfide mineralization (Fig. 13; T3: Thalhammer et al., 1986). A decrease in fluid temperature is also evident in the decreasing alteration intensity and rodingitization of Transform Sequence dykes, with the youngest "brownstone" dykes appearing less-altered relative to earlier amphibolite facies dykes (Murton 1986b). The proposed three-stage interpretation presented in this study for Lakxia tou Mavrou effectively links mineralogical, geochemical and isotopic observations to the tectonic and magmatic evolution of the Limassol Forest Complex and the accumulation of sulfide minerals below the seafloor.

The entire mineralized package at Lakxia tou Mavrou has later been affected by deformation events related to the younger the Pevkos fault leading to the localization of sulfide mineralization along WNW-trending structures, and hence to post-ocean-floor dismemberment of sulfide mineralization during faulting (Fig. 1A and B). This interpretation is implicit in previous work (Panayiotou, 1980; Foose et al., 1985; Thalhammer et al., 1986). However, given the extreme weakness of both the host serpentinite and sulfide minerals, and considering the combination of magmatism and high-temperature hydrothermal fluid conditions required to generate the mineral concentrations of this type, we propose that the apparent association of sulfide mineralization with WNW faulting is a secondary effect, and is not related to transform related E-W deformation and serpentinite shear zone formation.

An analogue for ultramafic-hosted SMS or Outokumpu-type VMS deposits?

Sulfide mineralization at Lakxia tou Mavrou provides insights into sub-seafloor processes in ultramafic-hosted SMS deposits. The area surrounding Lakxia tou Mavrou, specifically the hydrothermal alteration of

dykes and gabbroic plutons, the depletion of dykes in PGE's relative to mantle values and the high $\delta^{34}S$ values in sulfide blebs provides evidence that gabbroic intrusions and cross-cutting dykes are a source of metals and heat, a relationship that is only inferred in ultramafic-hosted SMS deposits (e.g., Petersen et al., 2009). The occurrence of Co-Pentlandite and chrome spinel at Lakxia tou Mavrou is comparable to ultramafic SMS deposits, with chrome spinel forming through the replacement of peridotite host rocks (Marques et al., 2006, Borodaev et al., 2007; Fouquet et al., 2010), supported at Lakxia tou Mavrou by the abundance of mesh textured sulfides. However, the occurrence of pyrrhotite and isocubanite at Lakxia tou Mavrou, that are comparatively rare in SMS deposits indicate that fluids had a lower fS_2 at Lakxia tou Mavrou relative to those typical in ultramafic-hosted SMS deposits (Firstova et al., 2016). Sulfur isotope ratios of sulfide minerals at Lakxia tou Mavrou show that limited mixing between seawater and hydrothermal fluids occurred, indicating the system was semi-closed with respect to seawater influx. This is distinctly different to SMS deposits, which are located at or near the seafloor where seawater mixing with hydrothermal fluid readily occurs producing largely positive $\delta^{34}S$ values in SMS deposits (Fig. 11). Largely the variation in sulfur isotope composition is a consequence of the formation of Lakxia tou Mavrou at deeper crustal depths (~3 km) where seawater mixing was more restricted. Given the amount of erosion (~3-4 km) that occurred in the Limassol Forest Complex, it remains unclear if Lakxia tou Mavrou sulfide mineralization once outcropped on the seafloor.

When comparing between Lakxia tou Mavrou and Outokumpu-type VMS deposits, clear differences and similarities exist. Firstly, sulfide mineralogy is comparable between deposit types, with isocubanite, pyrrhotite and arsenide minerals forming common mineral phases (Thalhammer et al., 1986; Peltonen et al., 2008). In Outokumpu-type deposits, solid-state remobilization of metals during metamorphism is inferred to be an important process in concentrating Ni, whereby Ni is remobilized from surrounding disseminated mineralization into massive ore zones (Peltonen et al., 2008). This remobilization leads to the formation of "proto" Cu-rich ore that is overprinted by later Ni-rich mineral assemblages (e.g., at Outokumpu). At Lakxia tou Mavrou, metamorphic overprinting, besides deformation that occurred within

606 the seafloor transform zone is minor or absent. Nickel, which is concentrated in Co-pentlandite and
607 associated with pyrrhotite at Lakxia tou Mavrou occurred early in the deposit paragenesis and is associated
608 with an initial high-temperature phase of fluid flow, and is not related to later metamorphic remobilization
609 (Thalhammer et al., 1986). Trace metal signatures at Lakxia tou Mavrou are broadly comparable to those
610 reported in Outokumpu-type VMS deposits that are depleted in Sb, Bi and Pb, reflecting the lower content
611 of these elements in ultramafic compared to mafic and felsic lithologies (Peltonen et al., 2008).

612 Mineralizing processes at Lakxia tou Mavrou appear to be a hybrid between ultramafic-hosted SMS
613 deposits and Outokumpu-type VMS deposits. The well-constrained tectonic environment in which Lakxia
614 tou Mavrou formed suggests that seafloor transform fault zones are a plausible environment for the
615 formation of Outokumpu-type deposits, however subsequent metamorphism is required to upgrade metal
616 tenors and form a "typical" Outokumpu-type deposit. Furthermore, our data indicates that whilst similarities
617 do exist between ultramafic-hosted SMS deposits and Lakxia tou Mavrou, the environment of formation
618 was different. Lakxia tou Mavrou formed at much deeper crustal depths in the region of ~3 km. Lakxia tou
619 Mavrou does however provide a useful and readily accessible analogue to understand the role of mafic
620 intrusions as a source of heat and metals in ultramafic-hosted SMS deposits.

621 ## Summary and conclusions

622 At Lakxia tou Mavrou sulfide minerals have an average sulfur isotope ($\delta^{34}S$) composition of <0‰, S/Se
623 ratios that are highly variable and a depletion in PGE's with an enrichment in Au indicating that
624 mineralization formed through hydrothermal processes. When compared with traditional VMS/SMS
625 deposits that form at or near the seafloor, mineralization at Lakxia tou Mavrou formed at deeper crustal
626 levels, ~3-4 km below the seafloor, highlighting the potential for replacement-style mineralization deep
627 below the seafloor in transform fault zones. The occurrence of Co-pentlandite, pyrrhotite and isocubanite
628 and enrichment of all sulfide minerals in Ni and Co relative to basalt-hosted VMS deposits in Troodos
629 indicate a Co and Ni enriched source such as the serpentinization of mantle peridotites. Transform Sequence

dyke and gabbro intrusions played an important role in generating heat and acidity to drive prolonged high-temperature low-pH hydrothermal circulation at Lakxia tou Mavrou. Sulfide blebs within these dykes contain very high $\delta^{34}S$ values, are depleted in PGE's relative to Troodos magmatic rocks and contain alteration rims, indicating the leaching of sulfide minerals in dykes provided and additional source of metals at Lakxia tou Mavrou.

Whilst some aspects of the sulfide mineralization at Lakxia tou Mavrou are comparable to SMS deposits hosted in ultramafic rocks, such as mineralogy and sulfide geochemistry, the mineralizing processes are not analogous between the two environments. This is especially true when considering sulfur isotope systematics where the $\delta^{34}S$ composition of Lakxia tou Mavrou sulfide minerals indicate that progressive TSR of seawater took place in a semi-closed system compared to open system conditions at the seafloor during SMS deposit formation. Our study confirms the importance of mafic intrusions as a source of heat and metals in sub-seafloor replacement-style sulfide mineralization in ultramafic rocks on the seafloor. Furthermore, we highlight the potential to form Outokumpu-type sulfide deposits below the seafloor in transform fault zones that are affected by late magmatic intrusions. A hybrid model between ultamafic-hosted SMS deposits and Outokumpu-type VMS deposits best explains the style of mineralization at Lakxia tou Mavrou and bridges the gap between these two deposit types.

Acknowledgments

This work was funded by the Natural Environment Research Council (NERC) grant NE/M010848/1 "TeaSe: Tellurium and Selenium Cycling and Supply" awarded to Cardiff University. JWJ acknowledges the support of the Canadian Research Chair program. The authors acknowledge the support of Andreas Zissimos from the Geological Survey Department of Cyprus. We thank Michael Green for his assistance in the field. Duncan Muir is thanked for his assistance on the SEM. Graham Layne and Glenn Piercey of the Micro Analysis Facility at Memorial University of Newfoundland are thanked for their assistance during SIMS analysis. We thank Mark Hannington and Hannah Grant for their constructive

reviews. We thank associate editor Jonathan Cloutier and editor-in-chief Larry Meinert for the editorial handling of this manuscript.

References

Allen, D.E., Seyfried, W.E., 2003, Compositional controls on vent fluids from ultramafic-hosted hydrothermal systems at mid-ocean ridges: An experimental study at 400°C, 500 bars: Geochimica et Cosmochimica Acta, v. 67, p. 1531–1542.

Allen, D.E., Seyfried, W.E., 2004, Serpentinization and heat generation: constraints from Lost City and Rainbow hydrothermal systems: Geochimica et Cosmochimica Acta, v. 68, p. 1347–1354.

Alt, J.C., 1994, A sulfur isotopic profile through the Troodos ophiolite, Cyprus: Primary composition and the effects of seawater hydrothermal alteration: Geochimica et Cosmochimica Acta, v. 58, p. 1825–1840.

Alt, J.C., Shanks, W.C., 2003, Serpentinization of abyssal peridotites from the MARK area, Mid-Atlantic Ridge: sulfur geochemistry and reaction modeling: Geochimica et Cosmochimica Acta, v. 67, p. 641–653.

Blounot, C.W., Dickson, F.W., 1969, The solubility of anhydrite (CaSO 4) in NaCl-H 2O from 100 to 450°C and 1 to 1000 bars: Geochimica et Cosmochimica Acta, v. 33, p. 227–245.

Bogdanov Y.A., Bortnikov N.S., Vikentev I.V., Gurvich E.G., Sagalevich A.M., 1997, A new type of modern mineral-forming system: Black smokers of the hydrothermal field at 14°45′N latitude, mid-atlantic ridge: Geology of Ore Deposits, v. 39, p. 57-87.

Bogdanov Y.A., Bortnikov N.S., Vikentev I.V., Lein Y.A., Gurvich E.G., Sagalevich A.M., Simonov V.A., Ikoskii S.V., Stavrova O.O., Apollonov V.N., 2002 Mineralogical-Geochemical Peculiarities of Hydrothermal Sulfide Ores and Fluids in the Rainbow Field Associated with Serpentinites, Mid-Atlantic Ridge (36°14' N): Geology of Ore Deposits, v. 44, p. 444-473.

677 Borodaev, Yu.S., Bryzgalov, I.A., Mozgova, N.N., Uspenskaya, T.Yu., 2007, Pentlandite and Co-
678 enriched pentlandite as characteristic minerals of modern hydrothermal sulfide mounds hosted by
679 serpentinized ultramafic rocks (Mid-Atlantic Ridge): Moscow University Geological Bulletin, v.
680 62, p. 85–97.

681 Brazilian Metals Group 2015, Annual Report 2015, (www.bmgl.com.au/investors/annual-reports).

682 Brueckner, S.M., Piercey, S.J., Layne, G.D., Piercey, G., Sylvester, P.J., 2015, Variations of sulphur
683 isotope signatures in sulphides from the metamorphosed Ming Cu(−Au) volcanogenic massive
684 sulphide deposit, Newfoundland Appalachians, Canada: Mineralium Deposita, v. 50,p. 619–640.

685 Cann, J.R., Blackman, D.K., Smith, D.K., McAllister, E., Janssen, B., Mello, S., Avgerinos, E., Pascoe,
686 A.R., Escartin, J., 1997, Corrugated slip surfaces formed at ridge–transform intersections on the
687 Mid-Atlantic Ridge: Nature, v. 385, p. 329–332.

688 Cannat, M., 1993, Emplacement of mantle rocks in the seafloor at mid-ocean ridges: Journal of
689 Geophysical Research: Solid Earth, v. 98, p. 4163–4172.

690 Cannat M., Fontaine F., Escartin J., 2010, Serpentinization and associated hydrogen and methane fluxes
691 at slow spreading ridges, in Rona P.A., Devey C.W., Dyment J., Murton B.J., ed. Diversity of
692 Hydrothermal Systems on Slow Spreading Ocean Ridges, 188, American Geophysical Union,
693 Geophysical Monograph Series, v. 188, p. 241-264, 9780875904788.

694 Charlou, J.L., Donval, J.P., Fouquet, Y., Jean-Baptiste, P., Holm, N., 2002, Geochemistry of high H2 and
695 CH4 vent fluids issuing from ultramafic rocks at the Rainbow hydrothermal field (36°14′N,
696 MAR): Chemical Geology, v. 191, p. 345–359.

697 Cherkashev, G.A., Ivanov, V.N., Bel'tenev, V.I., Lazareva, L.I., Rozhdestvenskaya, I.I., Samovarov,
698 M.L., Poroshina, I.M., Sergeev, M.B., Stepanova, T.V., Dobretsova, I.G., Kuznetsov, V.Yu.,
699 2013, Massive sulfide ores of the northern equatorial Mid-Atlantic Ridge: Oceanology, v. 53, p.
700 607–619.

701 Coltat, R., Boulvais, P., Riegler, T., Pelleter, E., Branquet, Y., 2021, Element distribution in the root zone
702 of ultramafic-hosted black smoker-like systems: Constraints from an Alpine analog: Chemical
703 Geology, v. 559, 119916.

704 Connelly, D.P., Copley, J.T., Murton, B.J., Stansfield, K., Tyler, P.A., German, C.R., Van Dover, C.L.,
705 Amon, D., Furlong, M., Grindlay, N. and Hayman, N., 2012, Hydrothermal vent fields and
706 chemosynthetic biota on the world's deepest seafloor spreading centre: Nature
707 communications, v. 3, p. 1-9.

708 Cook, N.J., Halls, C., Boyle, A.P., 1993, Deformation and metamorphism of massive sulphides at
709 Sulitjelma, Norway: Mineralogical Magazine, v. 57, p. 67–81.

710 Cox, S., Fagereng, A., MacLeod, C.J., 2021, Shear zone development in serpentinized mantle:
711 implications for the strength of oceanic transform faults: Journal of Geophysical Research: Solid
712 Earth, v. 126, p. 1-28.

713 Denny, A.R., Kelley, D.S. and Früh-Green, G.L., 2016, Geologic evolution of the Lost City hydrothermal
714 l field: Geochemistry, Geophysics, Geosystems, v. 17, p.375-394.

715 Deschamps, F., Godard, M., Guillot, S., Hattori, K., 2013, Geochemistry of subduction zone
716 serpentinites: Lithos, v. 178, p. 96–127.

717 Dubinina, E.O., Bortnikov, N.S., Stavrova, O.O., Kossova, S.A., 2020, Sulfur Isotope Fractionation
718 During Sulfide Generation in the Hydrothermal Submarine Systems: The Case of Logatchev,
719 Krasnov, and Rainbow Hydrothermal Fields, Mid-Atlantic Ridge: Geology of Ore Deposits, v.
720 62, p. 351–371.

721 Eckstrand, O.R., and Hulbert, L.J. 1987. Selenium and the source of sulphur in magmatic nickel and
722 platinum deposits [abs.]: Geological Association of Canada - Mineralogical Association of
723 Canada Annual Meeting, Program with Abstracts, 1987, v.12, p. 40.

724 Escartin, J., Mével, C., Petersen, S., Bonnemains, D., Cannat, M., Andreani, M., Augustin, N., Bezos, A.,
725 Chavagnac, V., Choi, Y. and Godard, M., 2017. Tectonic structure, evolution, and the nature of
726 oceanic core complexes and their detachment fault zones (13 20′ N and 13 30′ N, Mid Atlantic
727 Ridge): Geochemistry, Geophysics, Geosystems, v.18, p.1451-1482.

728 Escartín, J., Mével, C., MacLeod, C.J., McCaig, A.M., 2003, Constraints on deformation conditions and
729 the origin of oceanic detachments: The Mid-Atlantic Ridge core complex at 15°45′N:
730 Geochemistry, Geophysics, Geosystems, v. 4(8), p.1067.

731 Fagereng, A., MacLeod, C.J., 2019, On seismicity and structural style of oceanic transform faults: a field
732 geological perspective from the Troodos ophiolite, Cyprus, in Duarte, J.C. ed., Transform Plate
733 Boundaries and Fracture Zones, Elsevier Books, p. 437-459.

734 Firstova, A., Stepanova, T., Cherkashov, G., Goncharov, A., Babaeva, S., 2016, Composition and
735 Formation of Gabbro-Peridotite Hosted Seafloor Massive Sulfide Deposits from the Ashadze-1
736 Hydrothermal Field, Mid-Atlantic Ridge: Minerals, v. 6, p. 19.

737 Foose, M.P., Economou, M., Panayiotou, A., 1985, Compositional and mineralogic constraints on the
738 genesis of ophiolite hosted nickel mineralization in the Pevkos area, Limassol Forest, Cyprus:
739 Mineralium Deposita, v. 20, p. 234–240.

740 Fornari, D.J., Gallo, D.G., Edwards, M.H., Madsen, J.A., Perfit, M.R., Shor, A.N., 1989, Structure and
741 topography of the Siqueiros transform fault system: Evidence for the development of intra-
742 transform spreading centers: Marine Geophysical Researches, v. 11, p. 263–299.

743 Fouquet, Y., Cambon, P., Etoubleau, J., Charlou, J.L., Ondréas, H., Barriga, F.J.A.S., Cherkashov, G.,
744 Semkova, T., Poroshina, I., Bohn, M., Donval, J.P., Henry, K., Murphy, P., Rouxel, O., 2010,
745 Geodiversity of hydrothermal processes along the Mid-Atlantic Ridge and ultramafic-hosted
746 mineralization: A new type of oceanic Cu-Zn-Co-Au volcanogenic massive sulfide deposit, in

747 Rona, P.A., Devey, C.W., Dyment, J., Murton, B.J., ed., Geophysical Monograph Series,
748 American Geophysical Union, Washington, D.C., p. 321–367.
749 Fouquet, Y., Charlou J. L., Ondreas H., Radford-Knoery J., Donval J.P., Douville E., Apprioual R.,
750 Cambon P., Pelle H., Landure J.Y., Normand A., Ponzevera E., German C., Parson L., Barriga
751 F.J.A.S., Costa I., Relvas J., Ribeiro A., 1997, Discovery and first submersible on the Rainbow
752 hydrothermal field on the MAR (36º14'N): Eos Transactions, American Geophysical Union, 78,
753 832.
754 Francis, T.J.G., 1981, Serpentinization faults and their role in the tectonics of slow spreading ridges:
755 Journal of Geophysical Research: Solid Earth, v. 86, p. 11616–11622.
756 Früh-Green, G.L., Kelley, D.S., Bernasconi, S.M., Karson, J.A., Ludwig, K.A., Butterfield, D.A., Boschi,
757 C., Proskurowski, G., 2003, 30,000 Years of Hydrothermal Activity at the Lost City Vent Field:
758 Science v. 301, p. 495–498.
759 Gale, A., Dalton, C.A., Langmuir, C.H., Su, Y., Schilling, J.-G., 2013, The mean composition of ocean
760 ridge basalts. Geochemistry, Geophysics, Geosystems, v. 14, p. 489–518.
761 Gass, I.G., 1968. Is the Troodos Massif of Cyprus a Fragment of Mesozoic Ocean Floor? Nature, v. 220,
762 p. 39–42.
763 Gass, I. G., 1980, The Troodos Massif: Its Role in the Unravelling of the Ophiolite Problem and Its
764 Significance in the Understanding of Constructive Plate Margin Processes, in Malpas J., Moores,
765 E.M., Panayiotou, A. & Xenophontos, C., ed., Ophiolites: Ocean Crustal Analogues.
766 Proceedings of the International Ophiolite Symposium 1979, Geological Survey Department of
767 Cyprus, Nicosia, Cyprus, pp. 23–35.
768 Gass I.G. MacLeod C.J. Murton B.J. Panayiotou A. Simonian K.O. Xenophontos C., 1994, The Geology
769 of the Southern Troodos Transform Fault Zone: Nicosia, Cyprus, Geological Survey Department
770 Cyprus, Ministry of Agriculture, Natural Resources and Environment, Memoir 9, p. 218.

771 Gülaçar, O.F., Delaloye, M., 1976, Geochemistry of nickel, cobalt and copper in alpine-type ultramafic
772 rocks: Chemical Geology, v. 17, p. 269–280.

773 Hannington, M.D., de Ronde, C.D.J., Petersen, S., 2005, Sea-floor tectonics and submarine hydrothermal
774 systems, in Hedenquist, J.W., Thompson, J.F.H., Goldfarb, R.J., Richards, J.P. ed., Economic
775 Geology 100th Anniversary Volume. Society of Economic Geologists, Littelton, Colorado, USA,
776 p. 111–141.

777 Hannington, M.D., Bleeker, W., Kjarsgaard, I., 1999, Sulfide Mineralogy, Geochemistry, and Ore
778 Genesis of the Kidd Creek Deposit: Part II. The Bornite Zone*, in: Hannington, Mark D., Barrie,
779 C.T. ed., The Giant Kidd Creek Volcanogenic Massive Sulfide Deposit, Western Abitibi
780 Subprovince, Canada. Society of Economic Geologists, p. 225 - 266

781 Harris, D.C., Nickel, E.H., 1972, Pentlandite compositions and associations in some mineral deposits:
782 Canadian Mineralogist, v. 11, p. 861–878.

783 Hekinian, R., Bideau, D., Cannat, M., Francheteau, J., Hébert, R., 1992, Volcanic activity and crust-
784 mantle exposure in the ultrafast Garrett transform fault near 13°28′S in the Pacific: Earth and
785 Planetary Science Letters, v. 108, p. 259–275.

786 Huber, H., Koeberl, C., McDonald, I., Reimold, W.U., 2001, Geochemistry and petrology of
787 Witwatersrand and Dwyka diamictites from South Africa: search for an extraterrestrial
788 component: Geochimica et Cosmochimica Acta, v. 65, p. 2007–2016.

789 Huston, D.L., Sie, S.H., Suter, G.F., 1995, Selenium and its importance to the study of ore genesis: the
790 theoretical basis and its application to volcanic-hosted massive sulfide deposits using pixeprobe
791 analysis: Nuclear Instruments and Methods in Physics Research Section B: Beam Interactions
792 with Materials and Atoms, Nuclear Microprobe Technology and Applications, v. 104, p.476–480.

793 Ildefonse, B., Blackman, D.K., John, B.E., Ohara, Y., Miller, D.J., MacLeod, C.J., Integrated Ocean
794 Drilling Program Expeditions 304/305 Science Party, 2007, Oceanic core complexes and crustal
795 accretion at slow-spreading ridges: Geology, v. 35, p. 623–626.
796 Jowitt, S.M., Jenkin, G.R.T., Coogan, L.A., Naden, J., 2012, Quantifying the release of base metals from
797 source rocks for volcanogenic massive sulfide deposits: Effects of protolith composition and
798 alteration mineralogy: Journal of Geochemical Exploration, v. 118, p. 47–59.
799 Kampschulte, A., Strauss, H., 2004, The sulfur isotopic evolution of Phanerozoic seawater based on the
800 analysis of structurally substituted sulfate in carbonates: Chemical Geology, v. 204, p. 255–286.
801 Keith, M., Haase, K.M., Klemd, R., Krumm, S., Strauss, H., 2016, Systematic variations of trace element
802 and sulfur isotope compositions in pyrite with stratigraphic depth in the Skouriotissa volcanic-
803 hosted massive sulfide deposit, Troodos ophiolite, Cyprus: Chemical Geology, v. 423, p. 7–18.
804 Kelley, D.S., Karson, J.A., Blackman, D.K., Früh-Green, G.L., Butterfield, D.A., Lilley, M.D., Olson,
805 E.J., Schrenk, M.O., Roe, K.K., Lebon, G.T., Rivizzigno, P., 2001, An off-axis hydrothermal vent
806 field near the Mid-Atlantic Ridge at 30° N: Nature, v. 412, p. 145–149.
807 Klein, F., Bach, W., 2009, Fe–Ni–Co–O–S Phase Relations in Peridotite–Seawater Interactions: Journal
808 of Petrology, v. 50, p. 37–59.
809 Krasnov, S.G., Cherkashev, G.A., Stepanova, T.V., Batuyev, B.N., Krotov, A.G., Malin, B.V., Maslov,
810 M.N., Markov, V.F., Poroshina, I.M., Samovarov, M.S., Ashadze, A.M., Lazareva, L.I.,
811 Ermolayev, I.K., 1995, Detailed geological studies of hydrothermal fields in the North Atlantic:
812 Geological Society, London Special Publication, v. 87, p. 43–64.
813 Lafrance, B., Gibson, H.L., Stewart, M.S., 2020, Chapter 4: Internal and External Deformation and
814 Modification of Volcanogenic Massive Sulfide Deposits, in Rowland J.V., Rhys D.A. ed.,
815 Applied Structural Geology of ore-forming hydrothermal systems, Society of Economic
816 Geologists, Reviews in Economic Geology, v.21, pp. 147-171.

817 Layton-Matthews, D., Leybourne, M.I., Peter, J.M., Scott, S.D., Cousens, B., Eglington, B.M., 2013,
818 Multiple sources of selenium in ancient seafloor hydrothermal systems: Compositional and Se, S,
819 and Pb isotopic evidence from volcanic-hosted and volcanic-sediment-hosted massive sulfide
820 deposits of the Finlayson Lake District, Yukon, Canada: Geochimica et Cosmochimica Acta, v.
821 117, p. 313–331.

822 Leblanc, M., Billaud, P., 1982, Cobalt arsenide orebodies related to an upper Proterozoic ophiolite; Bou
823 Azzer (Morocco): Economic Geology, v. 77, p. 162–175.

824 Lein Yu.A., Ulyanova N.V., Ulyanov A.A., Cherkashev G.A., Stepanpva T.V., 2001, Mineralogy and
825 geochemistry of sulfide ores in ocean-floor hydrothermal fields associated with serpentinite
826 protrusions: Russian Journal of Earth Science, v. 3, p. 371-393

827 Liu, W., Borg, S.J., Testemale, D., Etschmann, B., Hazemann, J.-L., Brugger, J., 2011, Speciation and
828 thermodynamic properties for cobalt chloride complexes in hydrothermal fluids at 35–440°C and
829 600bar: An in-situ XAS study: Geochimica et Cosmochimica Acta, v. 75, p. 1227–1248.

830 Liu, W., Migdisov, A., Williams-Jones, A., 2012, The stability of aqueous nickel(II) chloride complexes
831 in hydrothermal solutions: Results of UV–Visible spectroscopic experiments: Geochimica et
832 Cosmochimica Acta, v. 94, p. 276–290.

833 Lode, S., Piercey, S.J., Layne, G.D., Piercey, G., Cloutier, J., 2017, Multiple sulphur and lead sources
834 recorded in hydrothermal exhalites associated with the Lemarchant volcanogenic massive
835 sulphide deposit, central Newfoundland, Canada: Mineralium Deposita, v. 52, p. 105-128.

836 MacDonald, A.H., Fyfe, W.S., 1985, Rate of serpentinization in seafloor environments: Tectonophysics,
837 Oceanic Lithosphere, v. 116, p. 123–135.

838 Machel, H.G., Krouse, H.R., Sassen, R., 1995, Products and distinguishing criteria of bacterial and
839 thermochemical sulfate reduction: Applied Geochemistry, v. 10, p. 373–389.

MacLeod, C.J., 1988, The Tectonic Evolution of the Eastern Limassol Forest Complex, Cyprus: Ph.D. Thesis, Milton Keynes, UK, The Open University, p. 368.

MacLeod, C.J., 1990, Role of the Southern Troodos Transform Fault in the rotation of the Cyprus microplate: evidence from the Eastern Limassol Forest Complex. In: Malpas J., Moores, E.M., Panayiotou, A. & Xenophontos, C., ed., Ophiolites: Ocean Crustal Analogues. Proceedings of the Symposium Troodos 1987, Geological Survey Department, Nicosia, Cyprus, p.75-85.

MacLeod, C.J., Allerton, S., Gass, I.G., Xenophontos, C., 1990, Structure of a fossil ridge–transform intersection in the Troodos ophiolite: Nature, v. 348, p. 717–720.

MacLeod, C.J., Escartín, J., Banerji, D., Banks, G.J., Gleeson, M., Irving, D.H.B., Lilly, R.M., McCaig, A.M., Niu, Y., Allerton, S., Smith, D.K., 2002, Direct geological evidence for oceanic detachment faulting: The Mid-Atlantic Ridge, 15°45′N: Geology, v. 30, p. 879–882.

MacLeod, C.J., Murton, B.J., 1993, Structure and tectonic evolution of the Southern Troodos Transform Fault Zone, Cyprus. Geological Society of London Special Publication, v. 76, p. 141–176.

MacLeod, C., Murton, B., 1995, On the sense of slip of the Southern Troodos Transform-Fault Zone, Cyprus: Geology, v. 23, p. 257-260.

Marques, A.F.A., Barriga, F., Chavagnac, V., Fouquet, Y., 2006. Mineralogy, geochemistry, and Nd isotope composition of the Rainbow hydrothermal field, Mid-Atlantic Ridge: Mineralium Deposita, v. 41, p. 52-67.

Marshall, B.,Gilligan, L.,1987, An introduction to remobilization: Information from ore-body geometry and experimental considerations: Ore Geology Reviews v. 2, p. 87–131.

Martin, A.J., Keith, M., McDonald, I., Haase, K.M., McFall, K.A., Klemd, R., MacLeod, C.J., 2019, Trace element systematics and ore-forming processes in mafic VMS deposits: Evidence from the Troodos ophiolite, Cyprus: Ore Geology Reviews, v. 106, p. 205–225.

Martin, A.J., Keith, M., Parvaz, D.B., McDonald, I., Boyce, A.J., McFall, K.A., Jenkin, G.R.T., Strauss, H., MacLeod, C.J., 2020, Effects of magmatic volatile influx in mafic VMS hydrothermal systems: Evidence from the Troodos ophiolite, Cyprus: Chemical Geology, v. 531, 119325.

Martin, A.J., McDonald, I., Jenkin, G.R.T., McFall, K.A., Boyce, A.J., Jamieson, J.W., MacLeod, C.J., 2021, A missing link between ancient and active mafic-hosted seafloor hydrothermal systems – Magmatic volatile influx in the exceptionally preserved Mala VMS deposit, Troodos, Cyprus. Chemical Geology, v. 567, 120127.

McCaig, A.M., Cliff, B., Escartín, J., Fallick, A.E., MacLeod, C.J., 2007, Oceanic detachment faults focus very large volumes of black smoker fluids: Geology, v. 35, p. 935-938.

McDonald, I., Viljoen, K.S., 2006, Platinum-group element geochemistry of mantle eclogites: a reconnaissance study of xenoliths from the Orapa kimberlite, Botswana: Applied Earth Science, v. 115, p. 81–93.

Melekestseva, I., Maslennikov, V., Tret'yakov, G., Maslennikova, S., Danyushevsky, L., Kotlyarov, V., Large, R., Beltenev, V., Khvorov, P., 2020, Trace Element Geochemistry of Sulfides from the Ashadze-2 Hydrothermal Field (12°58′ N, Mid-Atlantic Ridge): Influence of Host Rocks, Formation Conditions or Seawater? Minerals, v. 10, p. 743.

Melekestseva, I.Yu., Tret'yakov, G.A., Nimis, P., Yuminov, A.M., Maslennikov, V.V., Maslennikova, S.P., Kotlyarov, V.A., Beltenev, V.E., Danyushevsky, L.V., Large, R., 2014, Barite-rich massive sulfides from the Semenov-1 hydrothermal field (Mid-Atlantic Ridge, 13°30.87′ N): Evidence for phase separation and magmatic input: Marine Geology, v. 349, p. 37–54.

Mével, C., 2003. Serpentinization of abyssal peridotites at mid-ocean ridges. Comptes Rendus Geoscience, v. 335, p. 825–852.

885 Miyashiro, A., 1973, The Troodos ophiolitic complex was probably formed in an island arc, Earth and
886 Planetary Science Letters, v. 19, p. 218–224.

887 Moody, J.B., 1976, Serpentinization: a review: Lithos, v. 9, p.125-138.

888 Moores, E.M., Vine, F.J., Gast, P.W., Bullard, E.C., Cann, J.R., Matthews, D.H., 1971, The Troodos
889 Massif, Cyprus and other ophiolites as oceanic crust: evaluation and implications: Philosophical
890 Transactions of the Royal Society of London Mathematics and Physical Sciences, v. 268, p. 443–
891 467.

892 Mukasa, S.B., Ludden, J.N., 1987, Uranium-lead isotopic ages of plagiogranites from the Troodos
893 ophiolite, Cyprus, and their tectonic significance: Geology, v. 15, p. 825–828.

894 Murton, B.J., 1986a, Anomalous oceanic lithosphere formed in a leaky transform fault: evidence from the
895 Western Limassol Forest Complex, Cyprus: Journal of the Geological Society, v. 143, p. 845–
896 854.

897 Murton, B.J., 1986b, Tectonic evolution of the Western Limassol Forest Complex, Cyprus: Ph.D Thesis,
898 Milton Keynes, UK, The Open University, p. 198.

899 Naldrett, A.J., Duke, J.M., 1980, Platinum metals magmatic sulfide ores: Science, v. 208, p. 1417–1424.

900 Naldrett, A.J., Hoffman, E.L., Green, A.H., Chou, C.L., Naldrett, S.R., Alcock, R.A., 1979, The
901 composition of Ni-sulfide ores, with particular reference to their content of PGE and Au:
902 Canadian Mineralogist, v. 17, p. 403–415.

903 Ohmoto H., Rye R.O., 1979, Isotopes of sulfur and carbon. In: Geochemistry of Hydrothermal Ore
904 Deposits, in Barnes, H.L., ed., Geochemistry of hydrothermal ore deposit, 3rd edition: New York,
905 John Wiley and Sones, Inc., p. 509-567.

906 Ono, S., Keller, N.S., Rouxel, O., Alt, J.C., 2012, Sulfur-33 constraints on the origin of secondary pyrite
907 in altered oceanic basement: Geochimica et Cosmochima Acta, v. 87, p. 323–340.

908 Palme, H. and O'Neill, H.S.C., 2003, Cosmochemical estimates of mantle composition in Carlson R.W.,
909 ed., Tretaise in geochemistry, Vol. 2, The mantle and core pp.1-38. Oxford: Elsevier-Pergamon
910 Palandri, J.L., Reed, M.H., 2004. Geochemical models of metasomatism in ultramafic systems:
911 serpentinization, rodingitization, and sea floor carbonate chimney precipitation: Geochimica et
912 Cosmochimica Acta, v. 68, p. 1115–1133.

913 Panayiotou, A., 1980, Cu-Ni-Co-Fe sulphide mineralization, Limassol Forest, Cyprus, in Malpas J.,
914 Moores, E.M., Panayiotou, A. & Xenophontos, C., ed., Ophiolites: Ocean Crustal Analogues.
915 Proceedings of the International Ophiolite Symposium 1979, Geological Survey Department of
916 Cyprus, Nicosia, Cyprus, p. 102-116.

917 Parkkinen, J., Loukola-Ruskeeniemi, K. and Sorjonen-Ward, P., 1997, An outline of the history of
918 exploration and mining in the Outokumpu district: Research and exploration — where do they
919 meet? 4th Biennial SGA Meeting, August 11–13, 1997, Turku, Finland. Excursion guidebook
920 A4, Geological Survey of Finland, Guide, v. 42, p. 27-28.

921 Patten, C.G.C., Coltat, R., Junge, M., Peillod, A., Ulrich, M., Manatschal, G., Kolb, J., 2022, Ultramafic-
922 hosted volcanogenic massive sulfide deposits: an overlooked sub-class of VMS deposit forming
923 in complex tectonic environments: Earth-Science Reviews v. 224, 103891.

924 Pearce, J.A., 1975. Basalt geochemistry used to investigate past tectonic environments on Cyprus:
925 Tectonophysics, v. 25, p. 41–67.

926 Pearce, J.A., Robinson, P.T., 2010, The Troodos ophiolitic complex probably formed in a subduction
927 initiation, slab edge setting: Gondwana Research, v. 18, p. 60–81.

928 Peltonen, P., Kontinen, A., Huhma, H., Kuronen, U., 2008, Outokumpu revisited: New mineral deposit
929 model for the mantle peridotite-associated Cu–Co–Zn–Ni–Ag–Au sulphide deposits: Ore
930 Geology Reviews, v. 33, p. 559–617.

931 Petersen, S., Kuhn, K., Kuhn, T., Augustin, N., Hékinian, R., Franz, L., Borowski, C., 2009, The
932 geological setting of the ultramafic-hosted Logatchev hydrothermal field (14°45′N, Mid-Atlantic
933 Ridge) and its influence on massive sulfide formation: Lithos, v. 112, p. 40–56.

934 Prichard, H.M., Knight, R.D., Fisher, P.C., McDonald, I., Zhou, M.-F., Wang, C.Y., 2013, Distribution of
935 platinum-group elements in magmatic and altered ores in the Jinchuan intrusion, China: an
936 example of selenium remobilization by postmagmatic fluids: Mineralium Deposita, v. 48, p. 767–
937 786.

938 Prichard, H.M., Lord, R.A., 1990, Platinum and palladium in the Troodos ophiolite complex, Cyprus:
939 Canadian Mineralogist, v. 28, p. 607–617.

940 Queffurus, M., Barnes, S.-J., 2015, A review of sulfur to selenium ratios in magmatic nickel–copper and
941 platinum-group element deposits: Ore Geology Reviews, v. 69, p. 301–324.

942 Robertson, A.H.F., 1977, Tertiary uplift history of the Troodos massif, Cyprus: Geological Society of
943 America Bulletin, v. 88, p. 1763–1772.

944 Rona, P.A., Widenfalk, L., Boström, K., 1987. Serpentinized ultramafics and hydrothermal activity at the
945 Mid-Atlantic Ridge crest near 15°N: Journal of Geophysical Research: Solid Earth, v. 92, p.
946 1417–1427.

947 Rouxel, O., Fouquet, Y., Ludden, J.N., 2004, Copper Isotope Systematics of the Lucky Strike, Rainbow,
948 and Logatchev Sea-Floor Hydrothermal Fields on the Mid-Atlantic Ridge: Economic Geology, v.
949 99, p. 585–600.

950 Sakai, H., 1968, Isotopic properties of sulfur compounds in hydrothermal processes: Geochemical
951 Journal, v. 2, p. 29–49.

952 Seyfried, W.E., Mottl, M.J., 1982, Hydrothermal alteration of basalt by seawater under seawater-
953 dominated conditions. Geochimica et Cosmochimica Acta, v. 46, p. 985–1002.

954 Simonian, K.O., 1975. The Geology of the Arakapas Fault Belt Area Troodos Massif, Cyprus: Ph.D
955 thesis, Milton Keynes, UK, The Open University, pp. 151.

956 Simonian, K.O., Gass, I.G., 1978, Arakapas fault belt, Cyprus: A fossil transform fault. Geological
957 Society of American Bulletin, v. 89, p. 1220–1230.

958 Smith, J.W., Holwell, D.A., McDonald, I., Boyce, A.J., 2016, The application of S isotopes and S/Se
959 ratios in determining ore-forming processes of magmatic Ni–Cu–PGE sulfide deposits: A
960 cautionary case study from the northern Bushveld Complex: Ore Geology Reviews, v. 73, p. 148–
961 174.

962 Takai, K., Nakamura, K., Toki, T., Tsunogai, U., Miyazaki, M., Miyazaki, J., Hirayama, H., Nakagawa,
963 S., Nunoura, T., Horikoshi, K., 2008, Cell proliferation at 122°C and isotopically heavy CH4
964 production by a hyperthermophilic methanogen under high-pressure cultivation: Proceedings of
965 the National Academy of Sciences of the United States of America, v. 105, p. 10949–10954.

966 Tao, C., Seyfried, W.E., Lowell, R.P., Liu, Y., Liang, J., Guo, Z., Ding, K., Zhang, H., Liu, J., Qiu, L.,
967 Egorov, I., Liao, S., Zhao, M., Zhou, J., Deng, X., Li, H., Wang, H., Cai, W., Zhang, G., Zhou,
968 H., Lin, J., Li, W., 2020, Deep high-temperature hydrothermal circulation in a detachment
969 faulting system on the ultra-slow spreading ridge: Nature Communications, v. 11, 1300.

970 Thalhammer, O., Stumpfl, E.F., Panayiotou, A., 1986, Postmagmatic, hydrothermal origin of sulfide and
971 arsenide mineralizations at Limassol Forest, Cyprus: Mineralium Deposita, v. 21, p. 95–105.

972 Wang, Y., Han, X., Petersen, S., Frische, M., Qiu, Z., Cai, Y., Zhou, P., 2018, Trace Metal Distribution in
973 Sulfide Minerals from Ultramafic-Hosted Hydrothermal Systems: Examples from the Kairei Vent
974 Field, Central Indian Ridge: Minerals, v. 8, 526.

975 Yamamoto, M., 1976, Relationship between Se/S and sulfur isotope ratios of hydrothermal sulfide
976 minerals: Mineralium Deposita, v. 11, p. 197–209.

Figure Captions

Figure 1: Location map of Lakxia tou Mavrou and surrounding area. A) Location of the Southern Troodos Transform Fault Zone (STTFZ) on the island of Cyprus. B) Geological map of the STTFZ (delineated by the two dashed white lines) with major geological terranes that form the STTFZ highlighted (AFB = Arakapas Fault Belt, LFC= Limassol Forest Complex). C) The location of Lakxia tou Mavrou. D) Map showing the location of the sulfide mineralization at Lakxia tou Mavrou (after BMG, 2015). Coordinates in WGS 1984, Zone 36S.

Figure 2: Field photographs from Lakxia tou Mavrou. A) Sheared Transform Sequence dyke containing sulfide blebs (inset image). B) Sheared and boudinaged transform sequence dyke in serpentinite (arrows indicate shear sense). C) Serpentinite fabric showing dextral slip kinematics (E-W lineation) from the serpentinite shear zone. D) Contact between massive pyrrhotite and serpentinite in the historic adit (see Fig. 1B). E and F) Vein mineralization with a mesh of pyrrhotite, isocubanite and chalcopyrite (gray-yellow) in serpentinite (green-white) with a mylonitic texture. F*) Inset image showing close-up view of serpentinite (Serp.) clasts and sheared mylonitic sulfides. Red lines show serpeninite clasts with a crude sigmoidal shape. G) Massive pyrrhotite with disseminated chalcopyrite and Co-pentlandite from the exposed gossan.

Figure 3: Photomicrographs in reflected light of massive sulfide samples. A) Magnetite-bearing breccia zone in pyrrhotite. B) Ductile deformation in pyrrhotite exhibiting a “fingerprint” texture with minor magnetite. C) Chalcopyrite with lamella of isocubanite and pyrrhotite. D) Euhedral chrome spinel grain in pyrrhotite with pitting and alteration at the grain margin. Minor magnetite. E) False color element map of a massive sulfide sample. Disseminated Co-pentlandite is clearly visible as orange grains in pyrrhotite. Magnetite-bearing breccia zones with silicate material occur cross-cutting the sample. Cp = chalcopyrite (blue-purple in E), Po = pyrrhotite (pink), Crs = chrome spinel (green), Icb = isocubanite (not visible in E), Mag = magnetite (red-brown), Si = silica (green-brown).

Figure 4: Photomicrographs in reflected light of veined samples. A) Isocubanite associated with chalcopyrite, pyrrhotite and Co-pentlandite. B) Massive pyrrhotite and isocubanite with interstitial chalcopyrite. Co-pentlandite is associated with pyrrhotite. C) Euhedral chrome spinel surrounded by chalcopyrite, cubanite and minor pyrrhotite. D) Chrome spinel with a pitted appearance and a lighter colored alteration rim of ferri-chromite. E) Isocubanite being replaced by chalcopyrite at the contact with surrounding serpentinite. F) Chalcopyrite exsolution in isocubanite. G) Massive pyrrhotite. H) Close up image of feathery inclusions of Co-pentlandite in pyrrhotite. I) Chalcopyrite at the contact between pyrrhotite and serpentinite brecciated vein. J) Mesh textured veins of chalcopyrite and pyrrhotite. K) Serpentinite veins in pyrrhotite. L) Brittle deformation where individual sulfide grains appear fragmented. Po = pyrrhotite, Icb = isocubanite, Co-Pn = cobalt pentlandite, Cp = chalcopyrite, CrS = chrome spinel, Srp = serpentinite.

Figure 5: False color element maps of veined samples highlighting mineralogical and textural associations. A) Spatial association between pyrrhotite and pentlandite. Isocubanite has a massive texture whilst chalcopyrite occurs primarily as veins. Chrome spinel is associated with serpentinite. B) Development of a stockwork texture with a mesh of serpentinite veins. In contrast to image A, chalcopyrite occurs as aggregates of euhedral grains within massive isocubanite. C) Chalcopyrite localized along shear bands that cut isocubanite and pyrrhotite. Note crude sigmoidal shape to serpentinite “clasts”. Po = pyrrhotite, Icb = isocubanite, Co-Pn = cobalt pentlandite, Cp = chalcopyrite, CrS = chrome spinel, Srp = serpentinite.

Figure 6: Transform Sequence boninite dyke. A) Image in reflected light of a sulfide globule containing chalcopyrite, pyrrhotite and chrome spinel. B) Sulfide globule in reflected light containing pyrrhotite. C) False color element map showing micro-inclusions of pentlandite (inset image) and an alteration halo. D) Alteration halo surrounding pyrrhotite with chromite in silicate groundmass. Pn = pentlandite, Cp = chalcopyrite, Po = pyrrhotite, CrS = chrome spinel.

Figure 7: Trace element geochemistry analyzed via LA-ICP-MS (*n=185* spots) for isocubanite, chalcopyrite, pentlandite and pyrrhotite. A) Se, B) Te, C) Bi, D) Ni, E) Cu and F) Co. G) Co vs Ni. H) Zn

1025 vs. Cd. Full data in Appendix Table A1. Lower box (black) = 75th percentile, upper box (color) = 25th
1026 percentile, median = black line, whiskers = min and max value.

1027 Figure 8: Sulfur isotope composition ($\delta^{34}S$) analyzed via SIMS in pyrrhotite and chalcopyrite. Dyke-hosted
1028 pyrrhotite is notably enriched in ^{34}S relative to pyrrhotite at Lakxia tou Mavrou. Star = average, black line
1029 = median, lower box = 75th percentile, upper box = 25th percentile, whiskers = min and max value. Note
1030 varying Y-axis for dyke-hosted pyrrhotite.

1031 Figure 9: Chondrite normalized PGE plots. Red/blue/purple lines are data collected in this study for
1032 massive, veined samples and dyke samples. Gray regions represent Troodos magmatic rocks.
1033 Mineralization at Lakxia tou Mavrou is enriched in Au relative to Troodos igneous rocks (Troodos: Prichard
1034 and Lord, 1990; chondrite values Naldrett and Duke 1980).

1035 Figure 10: Cobalt/Ni ratios from the LA-ICP-MS analysis of pyrrhotite at Lakxia tou Mavrou and pyrite at
1036 the Skouriotissa VMS deposit (Martin et al., 2019). The median Co/Ni for harzburgite is 0.05 (*Gulaqar
1037 and Delaloye, 1976 and Deschamps 2013) whilst the sheeted dyke complex is 2 (** Jowitt et al., 2012).
1038 Lakxia tou Mavrou has lower Co/Ni ratios compared with Skouriotissa indicating an additional ultramafic
1039 source of these metals at Lakxia tou Mavrou.

1040 Figure 11: Sulfur isotope composition ($\delta^{34}S$) of sulfide minerals in ultramafic-hosted SMS deposits,
1041 Troodos VMS deposits, the basalt-hosted Mala VMS deposit (Troodos) and Lakxia tou Mavrou. TO =
1042 Troodos Ophiolite (data: Martin et al., 2021, 2020; Rouxel et al., 2004; Bogdanov et al., 1997, 2002; Lein
1043 et al., 2001, Melekestseva 2014; Firstova et al., 2016). Max = upper quartile (UQ) + 1.5* inter quartile
1044 range (IQR), Min = lower quartile (LQ) – 1.5* IQR.

1045 Figure 12: Schematic summary of sulfur isotope systematics at Lakxia tou Mavrou (not to scale). A)
1046 Seawater precipitates anhydrite when the temperature of the hydrothermal fluid is >150°C. B) Remaining
1047 sulfate in the fluid is transported to deeper crustal levels and, at temperatures >250°C, undergoes TSR
1048 forming H_2S. Sulfide minerals form when a small proportion of sulfate undergoes TSR (low *f* values ~0.1;

after Dubinina et al., 2020). The remaining sulfate in the fluid is enriched in ^{34}S relative to seawater sulfate (~18-19‰; Kampschulte and Strauss, 2004). C) Progressive TSR continues along a fluid flow pathway, forming sulfide minerals with progressively higher sulfur isotope values at high *f* values (~0.9) preserved in sulfide blebs (not to scale) from cross-cutting dykes.

Figure 13: Summary schematic for the formation of mineralization at Lakxia tou Mavrou. T1: Seawater penetrates deep into the crust (~3-4 km) along vertical serpentinite shear zones causing the serpentinization of mantle peridotites releasing Ni and Co. There is insufficient heat production to drive high-temperature hydrothermal circulation (>200 °C). T2: Intrusion of Transform Sequence plutons and early dyke swarms in the vicinity of Lakxia tou Mavrou producing widespread high-temperature (200-500°C) hydrothermal circulation. Anhydrite precipitates at temperatures >150°C and TSR occurs at temperatures >250°C. Where high-temperature metal-rich fluids mix with seawater-derived fluidS along E-W shear zone an initial high-temperature sulfide mineral assemblage of pyrrhotite and Co-pentlandite forms. Mesh textured pyrrhotite is common. Metals are leached from the margin of fractured gabbro intrusions and early dyke generations (inset image B). T3: Transform Sequence dyke intrusion. Dykes cross-cut both serpentinized harzburgite and gabbros. Dyke intrusion provides a renewed influx of heat driving lower temperature hydrothermal fluid circulation (200-300°C). Dykes provide an additional source of metals such as Cu forming an initial isocubanite-rich mineral assemblage that is then later overprinted by chalcopyrite. Chromite is altered to ferrichromite at its margins. Magmatic sulfide blebs are replaced by secondary pyrrhotite and chalcopyrite where sulfur is primarily sourced by the complete TSR of seawater (high *f* values) forming sulfide minerals that are enriched in ^{34}S up to 20.9‰ (inset image C).

Table Captions

Table 1: Summary of LA-ICP-MS data at Lakxia tou Mavrou for pyrrhotite, chalcopyrite, cubanite, Co-pentlandite and dyke-hosted pyrrhotite. Av = average, Med = median, σ = standard deviation, - = all

1073 analyses were blow the detection limit. Values below detection limit are taken as half the detection limit.
1074 See Appendix A1.

1075 Table 2: Platinum Group Element data from Ni fire assay for massive, veined and dyke material at Lakxia
1076 tou Mavrou. See Appendix 2.

1077

1078

1079

1080

1081

1082

1083

1084

1085

1086

1087

1088

1089

1090

1091

1092

1093 Figure 1:

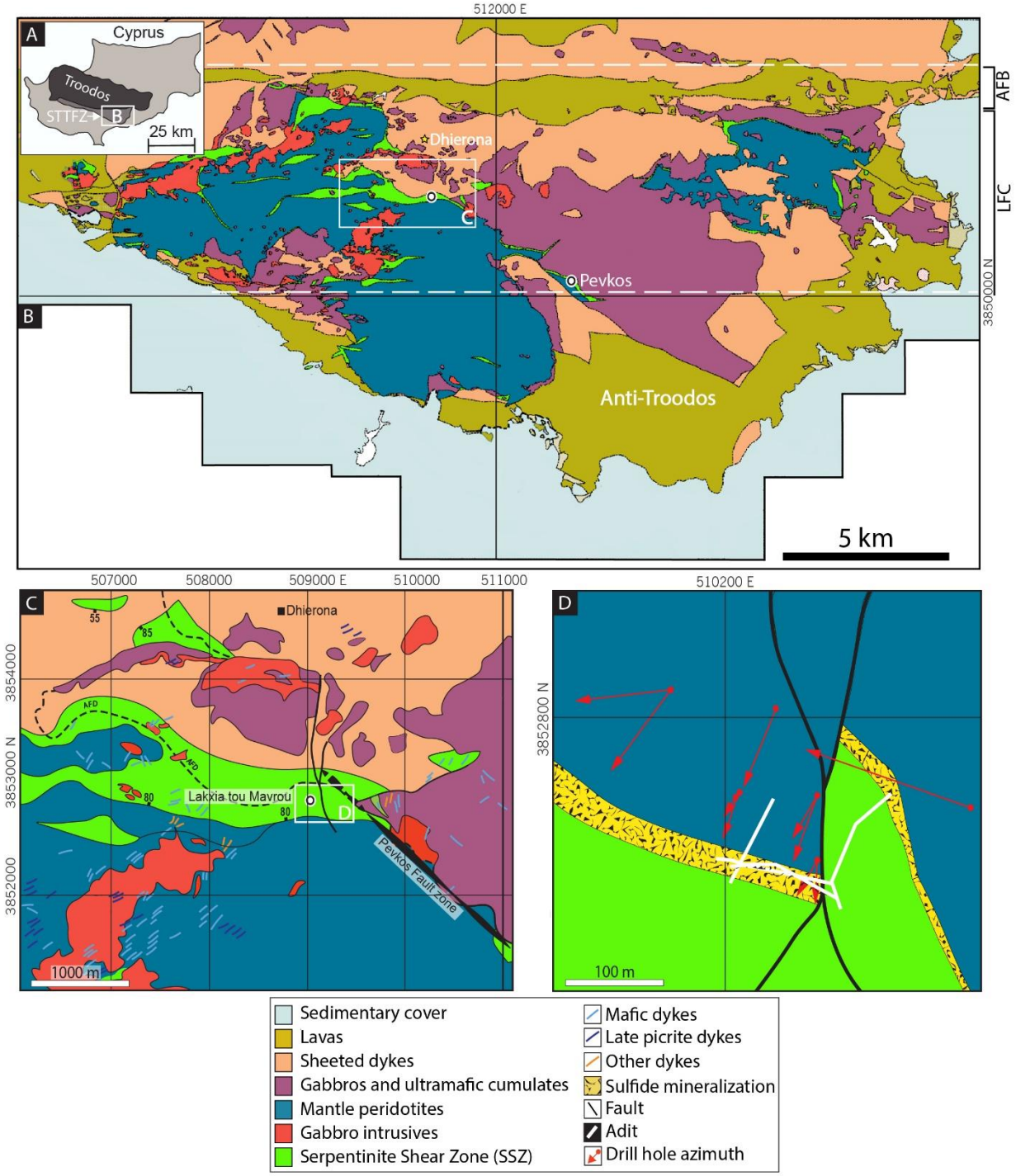

1094

1095

1096

Figure 2:

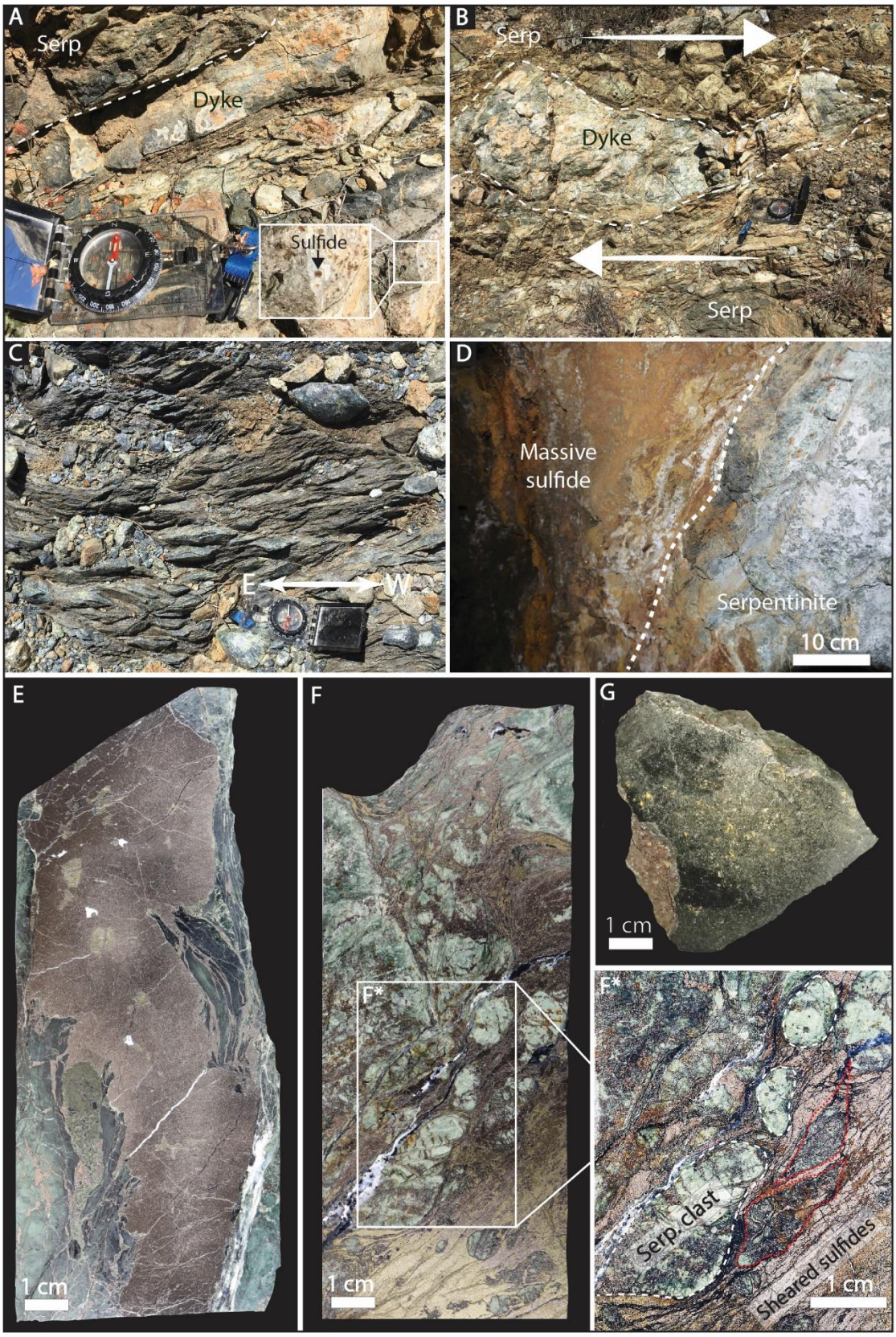
A
Serp
Dyke
Sulfide
B
Serp
Dyke
Serp
C
E
W
D
Massive sulfide
Serpentinite
10 cm
E
1 cm
F
F*
1 cm
G
1 cm
F*
Serp. clast
Sheared sulfides
1 cm

Figure 3:

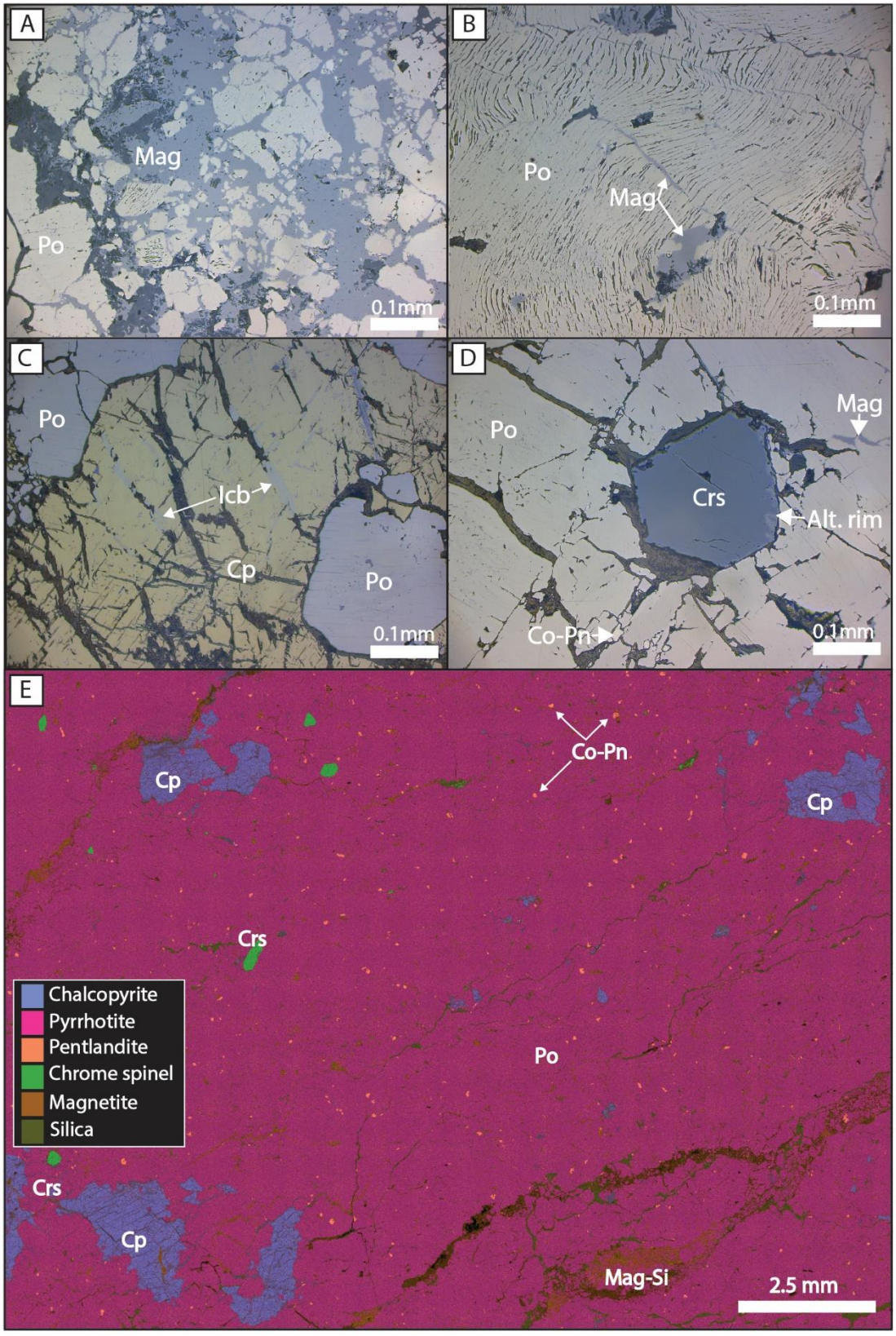
A
Mag
Po
0.1mm
B
Po
Mag
0.1mm
C
Po
Icb
Cp
Po
0.1mm
D
Mag
Po
Crs
Alt. rim
Co-Pn
0.1mm
E
Co-Pn
Cp
Cp
Crs
Chalcopyrite
Pyrrhotite
Pentlandite
Chrome spinel
Magnetite
Silica
Po
Crs
Cp
Mag-Si
2.5 mm

1157 Figure 4:

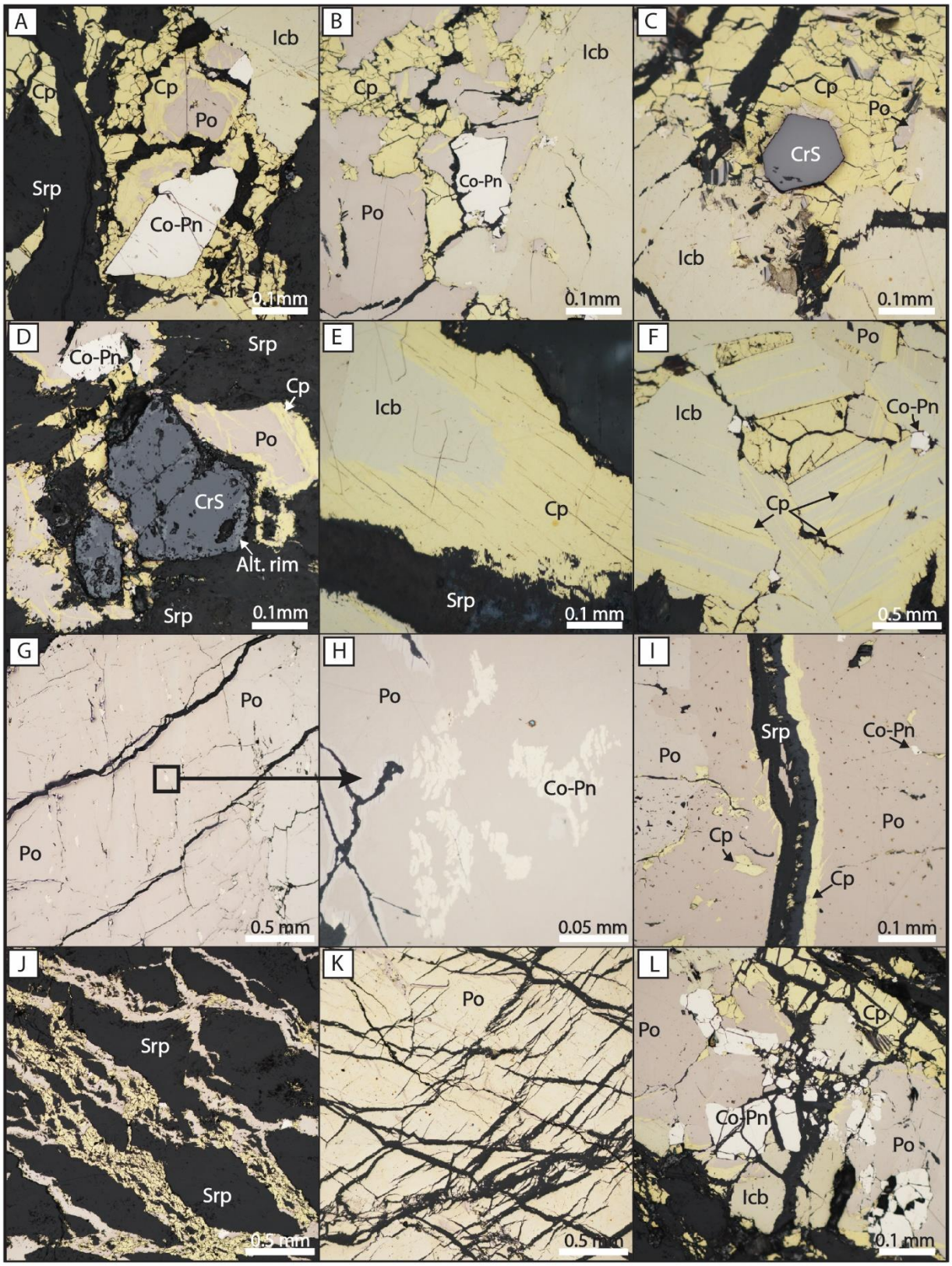

1158

1159 Figure 5:

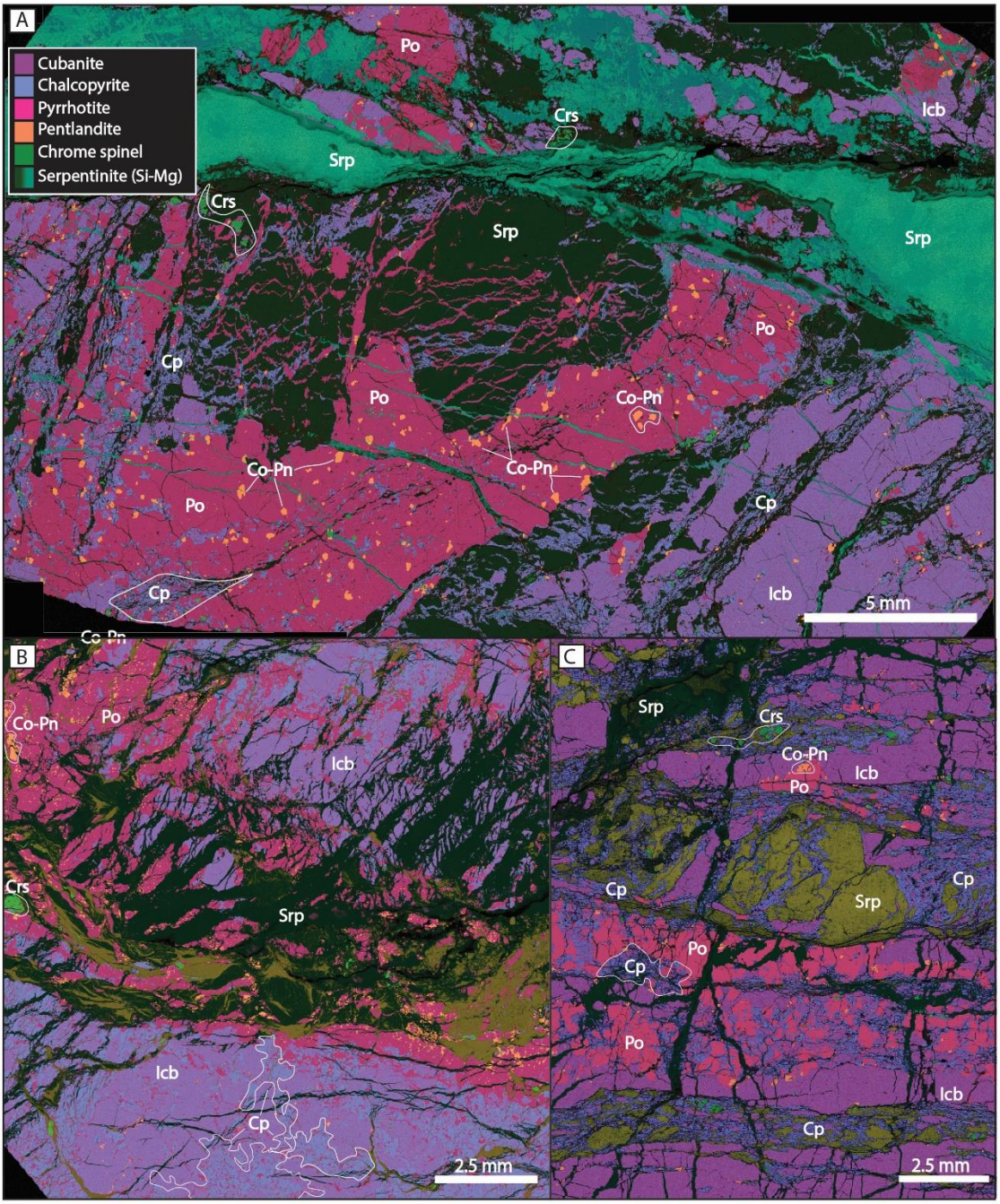

1160

1161

1162

1163

1164

1165

Figure 6:

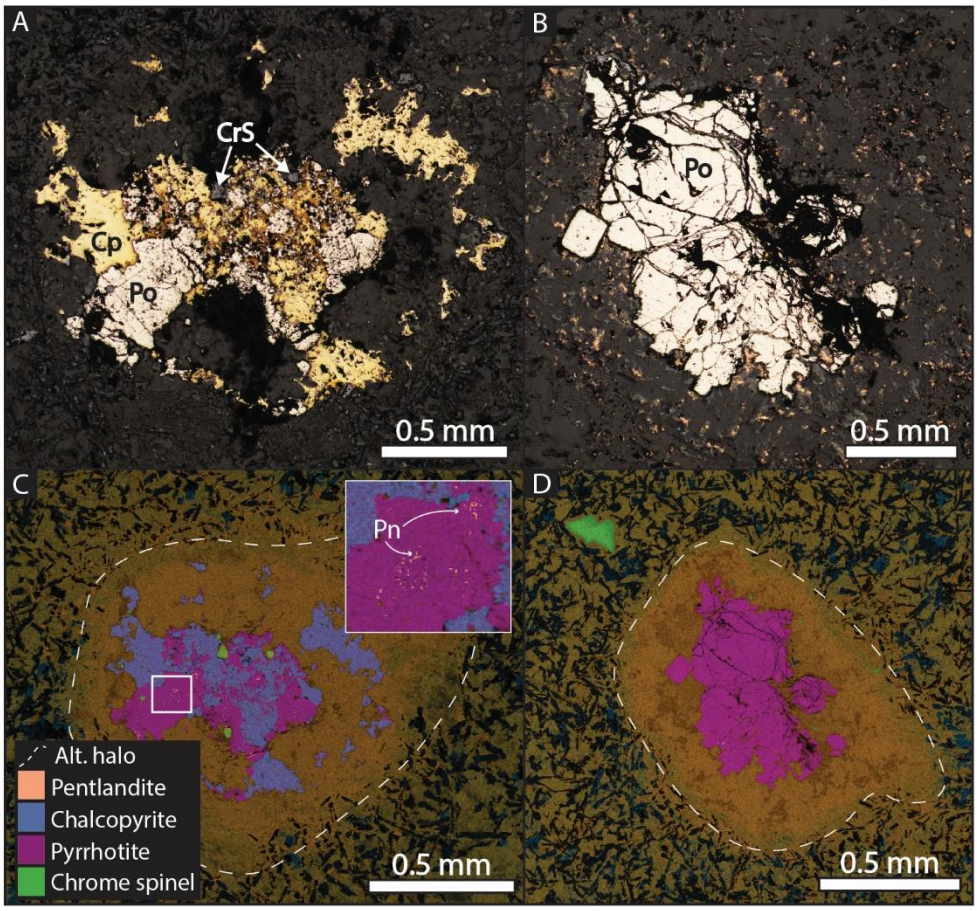
A
CrS
Cp
Po
0.5 mm
B
Po
0.5 mm
C
Pn
Alt. halo
Pentlandite
Chalcopyrite
Pyrrhotite
Chrome spinel
0.5 mm
D
0.5 mm

1180 Figure 7:

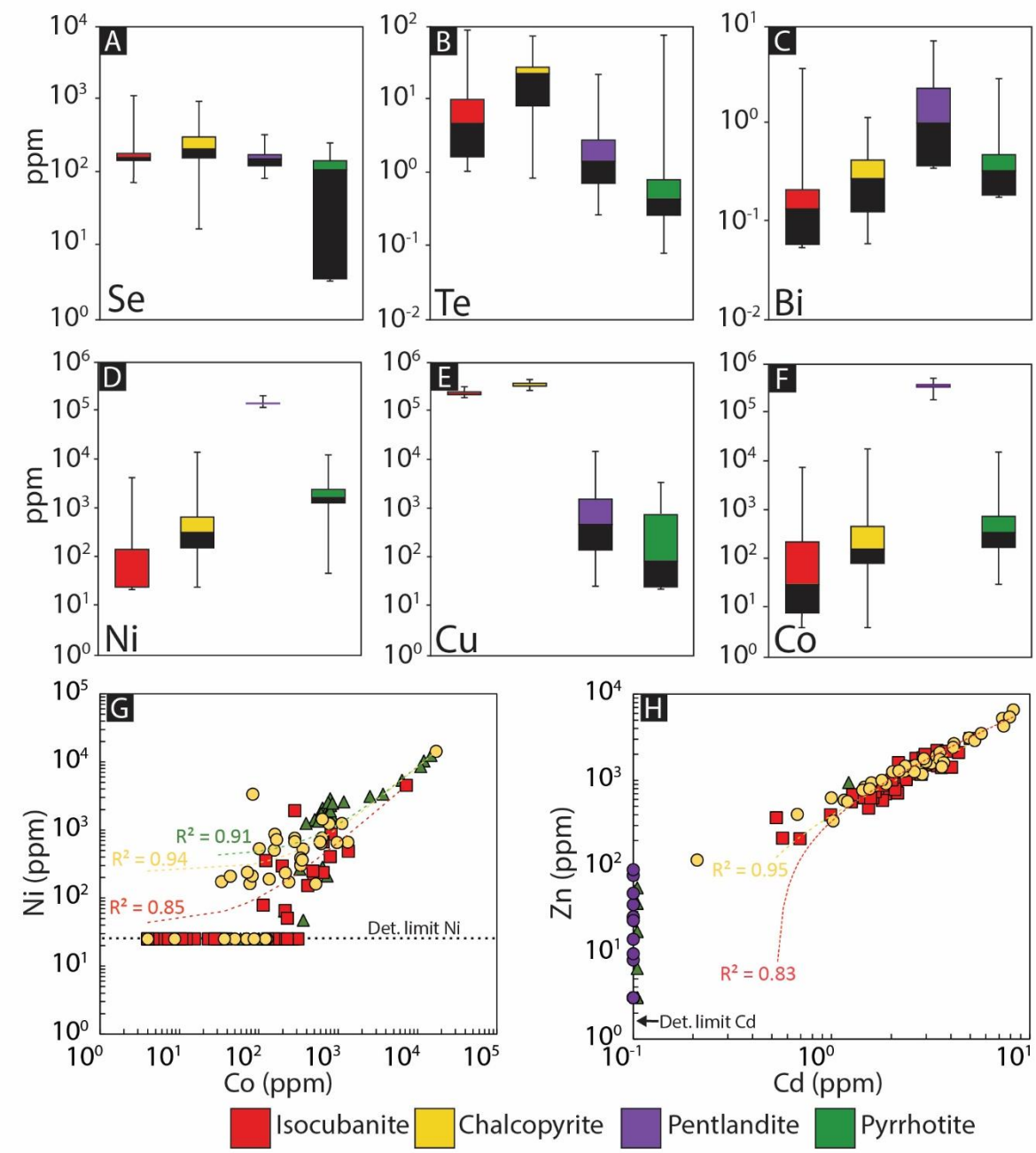

1181

1182

1183

1184

1185

1186

1187

1188 Figure 8:

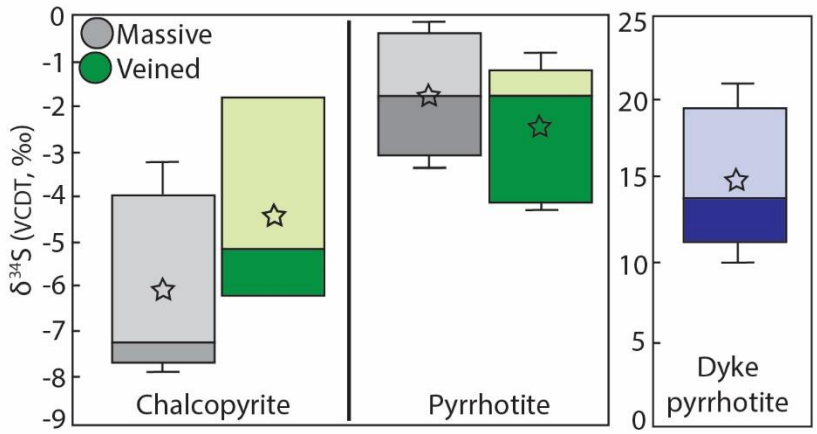

1197

1198 Figure 9:

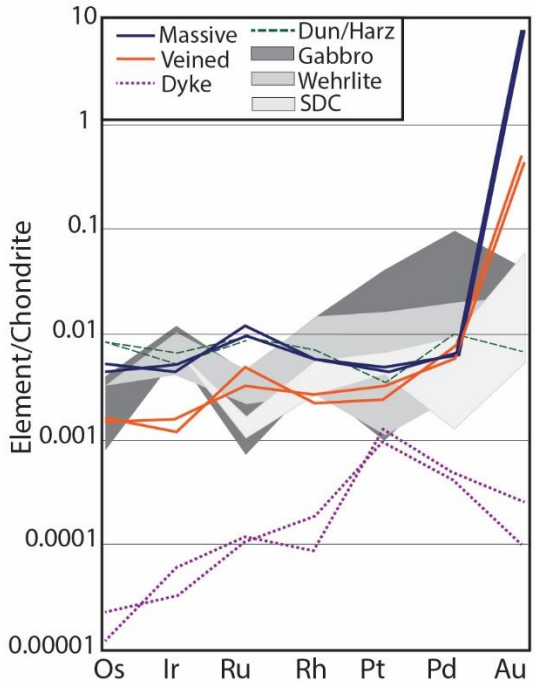

1199

1200

1201

1202

1203

1204

1205

1206 Figure 10:

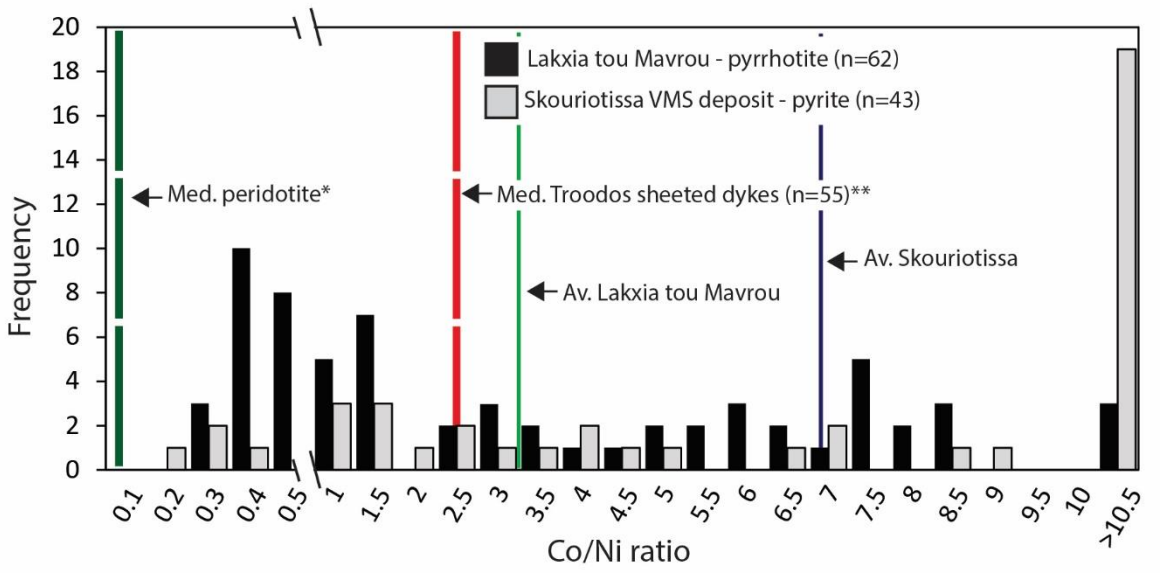

1207

1208

1209 Figure 11:

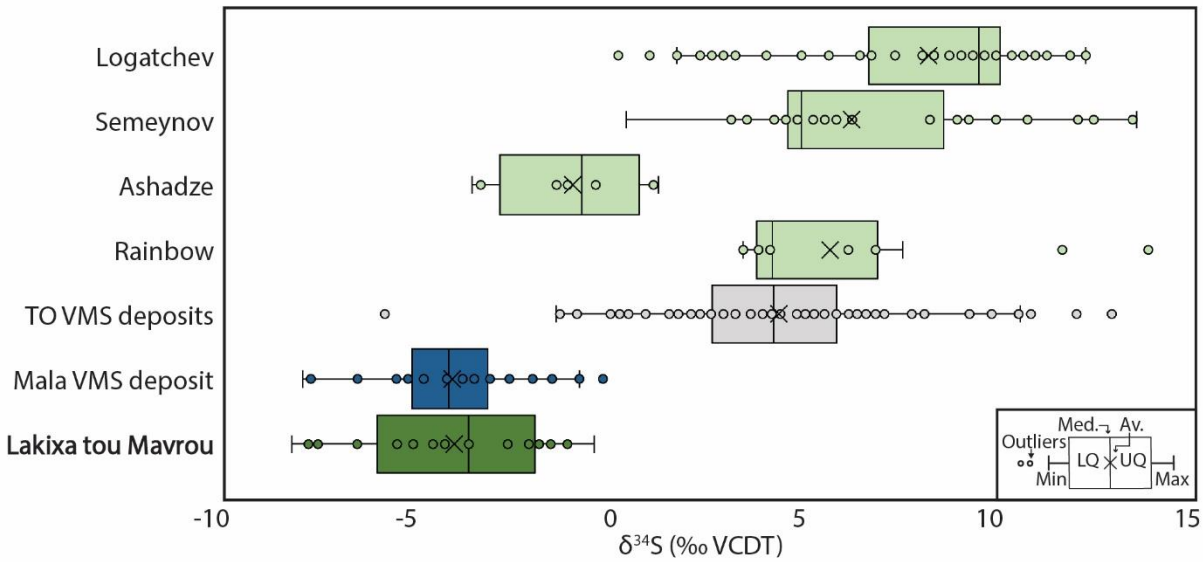

1210

1211

1212

1213

1214

1215

1216

Figure 12:

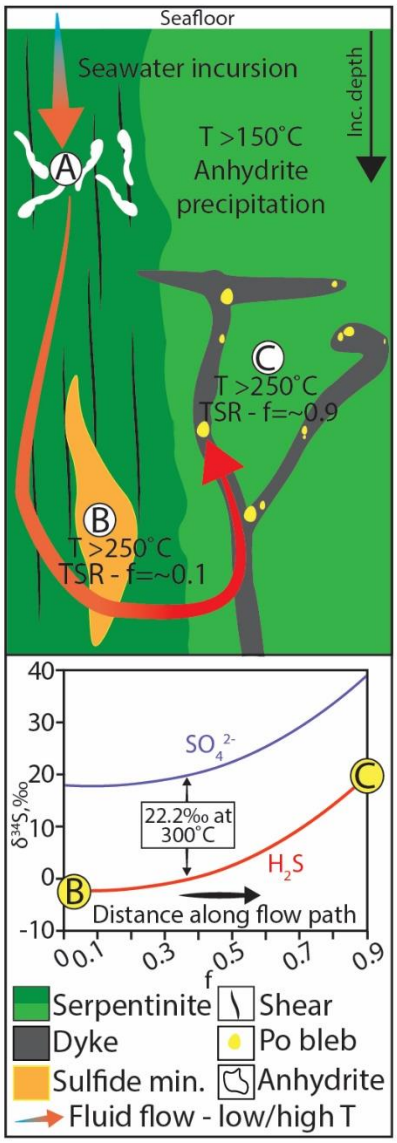
Seafloor
Seawater incursion
Inc. depth
T >150°C
Anhydrite
precipitation
A
C
T >250°C
TSR - f=~0.9
B
T >250°C
TSR - f=~0.1
40
30
20
10
0
-10
δ34S,‰
SO4 2-
22.2‰ at
300°C
H2S
C
B
Distance along flow path
0
0.1
0.3
0.5
0.7
0.9
f
Serpentinite
Dyke
Sulfide min.
Shear
Po bleb
Anhydrite
Fluid flow - low/high T

1227 Figure 13:

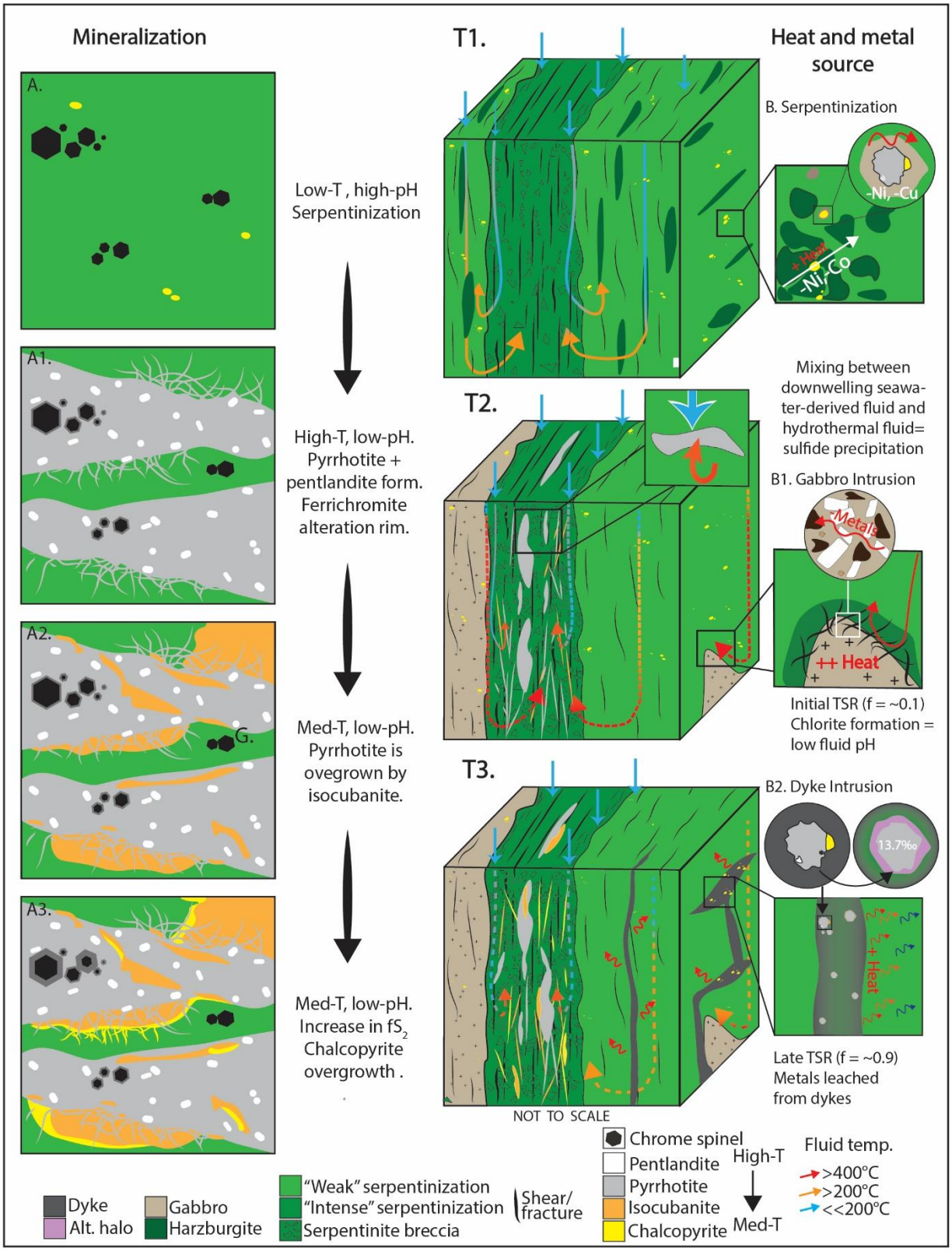

1228

1229 Table 1:

	S/Se	Fe	Co	Ni	Cu	Zn	As	Se	Ag	Cd	Sb	Te	Au	Pb	Bi
		wt%	ppm	ppm	wt%	ppm	ppm	ppm	ppm	ppm	ppm	ppm	ppm	ppm	ppm
Pyrrhotite	*n=62*														
Med.	3420	60.6	349	1706	0.01	3.0	-	111	0.08	0.11	0.07	0.44	0.01	1.20	0.33
Av.	37668	60.7	1173	2461	0.05	19.8	-	91.1	0.36	0.12	0.08	1.86	0.06	1.65	0.46
1σ	48314	2.02	2781	2372	0.07	119	-	76.7	1.10	0.14	0.12	9.85	0.16	1.90	0.51
Chalcopyrite	*n=38*														
Med.	1645	33.1	163.5	329	35.3	1451	-	213	0.26	2.75	0.40	22.6	0.01	1.20	0.27
Av.	3558	33.4	745	856	34.8	1840	-	262	0.72	3.14	1.51	21.1	0.02	1.29	0.31
1σ	5077	1.48	2673	146209	1.59	1423	-	208	1.42	1.97	2.99	14.9	0.01	0.52	0.25
Isocubanite	*n=45*														
Med.	2120	43.6	29.5	25.0	25.0	875	-	165	1.26	2.02	0.07	4.70	0.01	1.20	0.13
Av.	2045	43.1	339	250	25.6	1074	-	234	1.39	2.23	0.23	10.6	0.01	1.51	0.23
1σ	749	2.31	1081	724	2.55	610	-	231	0.76	1.00	0.58	16.5	0.03	1.52	0.54
Co-Pentlandite	*n=34*														
Med.	2188	23.3	345095	150931	0.05	3.0	21.9	153.1	0.08	-	0.23	1.44	0.01	1.20	1.01
Av.	2272	23.9	330001	18897	0.19	12.8	21.9	162.3	0.24	-	0.69	3.45	0.09	1.20	1.66
1σ	681	2.96	59164	1.89	0.34	21.5	5.04	55.5	0.37	-	1.03	5.41	0.26	0.00	1.76
Dyke pyrrhotite	*n=6*														
Med.	3422	60.1	542.1	1706	0.003	3.00	0.55	111	0.08	0.11	0.07	0.43	0.01	1.20	0.35
Av.	40088	59.4	1363.4	2461	0.04	22.6	6.03	93.0	0.38	0.12	0.08	2.32	0.07	1.83	0.49
1σ	48299	7.80	2821.2	2809	0.06	121	19.9	82.4	1.12	0.14	0.13	10.1	0.16	2.01	0.52

1230

1231

1232 Table 2:

	Os	Ir	Ru	Rh	Pt	Pd	Au
	ppb	ppb	ppb	ppb	ppb	ppb	ppb
Vein	1.20	1.23	3.48	0.59	4.96	5.27	74.3
Vein	1.27	0.95	5.44	0.51	4.08	6.45	85.0
Massive	3.28	3.66	9.64	1.33	7.66	6.00	1090
Massive	3.75	3.23	12.1	1.28	6.98	5.77	1146
Dyke	0.02	0.03	0.14	0.05	1.65	0.43	0.03
Dyke	0.01	0.06	0.16	0.02	2.08	0.50	0.07

1233